

Low mass young stars in the Milky Way unveiled by DBSCAN and *Gaia* EDR3. Mapping the star forming regions within 1.5 Kpc

L. Prisinzano¹, F. Damiani¹, S. Sciortino¹, E. Flaccomio¹, M. G. Guarcello¹, G. Micela¹, E. Tognelli², R. D. Jeffries³, and J. M. Alcalá⁴

¹ INAF - Osservatorio Astronomico di Palermo, Piazza del Parlamento 1, 90134, Palermo, Italy

e-mail: loredana.prisinzano@inaf.it

² CEICO, Institute of Physics of the Czech Academy of Sciences, Na Slovance 2, 182 21 Praha 8, Czechia

³ Astrophysics Group, Keele University, Keele, Staffordshire ST5 5BG, United Kingdom

⁴ INAF - Osservatorio Astronomico di Capodimonte, via Moiariello 16, 80131 Napoli, Italy

ABSTRACT

Context. With an unprecedented astrometric and photometric data precision, *Gaia* EDR3 gives us, for the first time, the opportunity to systematically detect and map in the optical bands, the low mass populations of the star forming regions (SFRs) in the Milky Way. **Aims.** We provide a catalogue of the *Gaia* EDR3 data (photometry, proper motions and parallaxes) of the young stellar objects (YSOs) identified in the Galactic Plane ($|b| < 30^\circ$) within about 1.5 kpc. The catalogue of the SFRs to which they belong is also provided to study the properties of the very young clusters and put them in the context of the Galaxy structure.

Methods. We applied the machine learning unsupervised clustering algorithm DBSCAN on a sample of *Gaia* EDR3 data photometrically selected on the region where very young stars ($t \lesssim 10$ Myr) are expected to be found, with the aim to identify co-moving and spatially consistent stellar clusters. A subsample of 52 clusters, selected among the 7323 found with DBSCAN, has been used as template data set, to identify very young clusters from the pattern of the observed color-absolute magnitude diagrams through a pattern match process.

Results. We find 124 440 candidate YSOs clustered in 354 SFRs and stellar clusters younger than 10 Myr and within $\lesssim 1.5$ Kpc. In addition, 65 863 low mass members of 322 stellar clusters located within ~ 500 pc and with ages $10 \text{ Myr} \lesssim t \lesssim 100 \text{ Myr}$ were also found.

Conclusions. The selected YSOs are spatially correlated with the well known SFRs. Most of them are associated with well concentrated regions or complex structures of the Galaxy and a substantial number of them have been recognized for the first time. The massive SFRs, such as, for example, Orion, Sco-Cen and Vela, located within 600-700 pc trace a very complex three-dimensional pattern, while the farthest ones seem to follow a more regular pattern along the Galactic Plane.

Key words. methods: data analysis – stars: formation, pre-main sequence – Galaxy: open clusters and associations: general – catalogs – surveys

1. Introduction

It is by now well known that stars originate from collapse of cold molecular clouds, and mainly form in over-dense structures and clusters usually designated as star forming regions (SFRs). During the very early phases, young stellar objects (YSOs) can be identified in the near, mid far infrared (IR) and radio wavelengths because of the presence of the optically thick infalling envelope or circumstellar disk around the central star. In the subsequent pre-main sequence stage phase, they become visible also in the optical bands. But, when the final dispersal of the disk material occurs and non-accreting transition disks form, YSOs can no longer be identified in IR or radio surveys (Ercolano et al., 2021) and a complete census is possible only in the optical bands.

While a clean identification of YSOs is very hard using only optical photometry, an efficient way to systematically single out SFRs is by the identification of kinematical stellar groups having a common space motion. With an unprecedented astrometric precision and sky coverage, *Gaia* data offer the possibility to recognise the SFRs as common proper motion groups, at least within the *Gaia* observational limits.

Data from the *Gaia* mission are revolutionising our capability to map the youngest stellar populations of the Milky Way in the optical bands, which is one of the main core science goals for an overall understanding of the Galactic components. The youngest stellar component is crucial to better characterize the Galactic thin disk, and its spiral arms and to understand its origin.

The characterisation of individual SFRs and their dynamics are also fundamental to understand the local formation, evolution and dispersion of star clusters, as well as the star formation history and the Initial Mass Function. Finally, statistical studies of YSOs during the early years of their formation, when the proto-planetary discs are evolving and planets form, are crucial to shed light on planet formation theory.

With more than 1.3 billion stars with precise proper motions and astrometric (positions and parallaxes) and photometric measurements, *Gaia* DR2 data allowed several studies aimed to identify clustered populations of the Milky Way. Some of these studies have been dedicated to SFRs, associations and moving groups. Zari et al. (2018) presented an analysis of the clustered and diffuse young populations within 500 pc, using

a combination of photometric and astrometric criteria. Analogously, Kerr et al. (2021) studied the solar neighbourhood by applying the HDBSCAN clustering algorithm (McInnes et al., 2017). They found 27 young groups, associations and significant substructures, associated to known clusters and SFRs, and released a catalogue including $\sim 3 \times 10^4$ *Gaia* DR2 YSOs within 333 pc.

Cantat-Gaudin et al. (2018) started from a list of known clusters to assign them unsupervised membership and parameters. Other studies have been dedicated to systematically find open clusters in the Galaxy. Castro-Ginard et al. (2018) used the DBSCAN algorithm (Ester et al., 1996) to select a list of candidate open clusters (OC) which they then refined to identify real OCs with a well defined main sequence (MS). Other papers have been recently published to both discover new open clusters and derive their parameters (e.g. Cantat-Gaudin & Anders, 2020; Cantat-Gaudin et al., 2020; Castro-Ginard et al., 2020; Liu & Pang, 2019).

A recent attempt to find Galactic Plane (GP) clustered populations, including SFRs, has been made by Kounkel & Covey (2019) and Kounkel et al. (2020), again using *Gaia* DR2 data and the HDBSCAN unsupervised algorithm in 5D space ($l, b, \pi, \mu_{\alpha^*}, \mu_{\delta}$). In these works, the first limited to 1 Kpc and the second to 3 Kpc, they found clustered populations but also associations, moving groups and string-like structures, parallel to the GP, spanning hundreds of parsec in length. Clusters aged between 10 Myr and 1 Gyr have been found, with an onion-like approach, i.e. using the entire catalogue with different cutoffs in parallax and progressively merging the different catalogues.

A different approach has been adopted by Bica et al. (2019) who used infrared (IR) data from 2MASS, *WISE*, *VVV*, *Spitzer*, and *Herschel* surveys to compile a catalog of 10 978 Galactic star clusters, and associations, including 4 234 embedded clusters.

With the advent of *Gaia* Early Data Release 3 (EDR3), based on 34 months of observations¹, available photometric and astrometric measurements improved significantly. In particular, photometric improvements have been made in the calibration models, in the different photometric systems and in the treatment of the BP and RP local background flux (Riello et al., 2021).

In this paper, we use *Gaia* EDR3 data to systematically identify the low mass component of SFRs in the Galaxy, with ages approximately < 10 Myr and within a distance limit of ~ 1.5 Kpc, imposed by our data selection. We focus our analysis on very young clusters, by exploiting the significant progress achieved with *Gaia* EDR3 data. A full exploitation of the *Gaia* data and the results presented here would require further data, such as spectroscopic determination of individual stellar parameters, such as effective temperatures, gravities, and stellar luminosities as well as rotational and radial velocities, crucial to derive masses, ages and 3D space velocities. Even though the results presented here cannot be used at this stage to determine the IMF, Star Formation history and 3D kinematics of the SFRs, they can serve to trace the very young Galactic stellar component within 1.5-2 Kpc through a systematic method that homogeneously identifies the bulk population of the SFRs. Such results can be used both for statistical as well as for individual detailed analyses. The paper is organised as follows: we describe in Sect. 2 the requirements adopted to select the *Gaia* EDR3 data and in Sect. 3 the photometric selection applied to obtain the starting sample of the YSO candidates. In Sect. 4 we describe the method adopted to identify SFRs and stellar clusters, the criteria adopted to validate them and the age classification.

Our results and the discussion are presented in Sect. 5 and 6, respectively; finally, our summary and conclusions are presented in Sect 7. In the Appendix A we show the effects of the reddening in the *Gaia* color-absolute magnitude diagrams, in the Appendix B we estimate the effect of multiplicity in the selection of the YSOs while in the Appendix C we describe the comparison of specific regions with the literature.

2. *Gaia* data

In this analysis, we use the *Gaia* EDR3 data (Gaia Collaboration et al., 2016, 2021) which provide precise astrometry and kinematics ($l, b, \pi, \mu_{\alpha^*}, \mu_{\delta}$) as well as excellent photometry in three broad bands (G, G_{BP}, G_{RP}). Since our analysis is focused on the Galactic midplane, where most of the YSOs are expected to be found, we selected sources within $|b| < 30^\circ$. We limit our selection to $7.5 < G \leq 20.5$. The limit $G = 7.5$ has been chosen to discard objects with magnitudes derived from saturated CCD images, while $G = 20.5$ is the limit to include most of the objects with magnitude G uncertainties lower than 0.2 mag. This range includes the young low mass populations ($0.1 \lesssim M/M_{\odot} \lesssim 1.5$) of the known SFRs within the distance set by the limiting magnitude. In addition, we considered only positive parallax values. This choice does not introduce any bias since we do not expect to investigate stars with very small parallaxes that could have negative values (Luri et al., 2018). Finally, we imposed a relative parallax error lower than 20%, to discard stars with a poorly constrained distance, and, to take into account the *Gaia* EDR3 systematics, we also considered the renormalized unit weight error (RUWE), (Lindegren et al., 2021b), expected to be < 1.4 for sources where the single-star model provides a good fit to the astrometric observations.

To summarise, data of our interest were selected from the Astronomical Data Query Language (ADQL) interface of the ESA *Gaia* Archive² using the following restrictions:

$$\begin{cases} |b| < 30^\circ \\ 7.5 < G \leq 20.5 \\ \pi > 0 \text{ mas} \\ \sigma(\pi)/\pi < 0.2 \\ RUWE < 1.4 \end{cases} \quad (1)$$

We included in the query also a photometric condition aimed to include the Pre-Main Sequence (PMS) region of the M_G vs. $G - G_{RP}$ color-absolute magnitude diagram (CAMD) where all very young stars ($t \lesssim 10$ Myr) are expected to be found. We split our selection in two samples, namely bright and faint, according to the following criteria:

$$\text{Bright sample} = \begin{cases} M_G < 7.64(G - G_{RP}) + 0.22 \\ 5 < M_G \leq 9 \\ (G - G_{RP}) > 0.58 \end{cases} \quad (2)$$

$$\text{Faint sample} = \begin{cases} M_G < 15.00(G - G_{RP}) - 8.25 \\ M_G > 9 \\ (G - G_{RP}) > 0.58. \end{cases} \quad (3)$$

These limits are drawn as solid blue and green lines in Fig. 1. We note that in this work, for the reddening uncorrected absolute

¹ *Gaia* DR2 data were based on 22 months of observations

² <https://gea.esac.esa.int/archive/>

magnitudes, we adopted the definition $M_G = G + 5 \text{Log}(\pi) - 10$, based on the inverted *Gaia* EDR3 parallaxes, since, as shown in Piecka & Paunzen (2021), within <2 kpc, the inverse-parallax method gives results comparable to distances derived by the Bayesian approach (Bailer-Jones et al., 2021).

The minimum value $M_G = 5$ was set to avoid the upper region of the color-absolute magnitude diagram, where the overlap of the Upper MS or PMS stars of the SFRs with giants, MS or Turn-off stars, is expected to be very high, especially if the reddening is not corrected. This implies a cut of the massive population of the SFRs but it does not represent an issue for our investigation since we are mainly interested in the rich low mass component of these populations.

In order to further reduce the fraction of contaminants we used also the condition $G - G_{RP} > 0.58$, that is the minimum expected unreddened color for low mass ($M \lesssim 1.2 M_\odot$) PMS (age ≤ 10 Myr) stars.

Our photometric selection as well as the subsequent analysis are based on the $G - G_{RP}$ colors. This choice allows us to avoid the use of the G_{BP} magnitudes that for $G \gtrsim 20$ are strongly affected by the application of the minimum flux threshold, which overestimates the mean BP flux. This issue also affects the RP flux, but with a considerably lower effect in G_{RP} than in G_{BP} (Riello et al., 2021).

Once the data have been retrieved by the ESA *Gaia* Archive, parallax values were corrected by the zero point bias reported in Lindegren et al. (2021a), using the Python code available to the community³, that is a function of source magnitude, colour, and celestial position.

In addition, we performed a further data filtering by considering only objects with error in the $G - G_{RP}$ smaller than 0.14 mag. Standard errors in the magnitudes were computed by using the propagations of the flux errors with the formulas:

$$\sigma(G) = \sqrt{(-2.5/\ln(10)\sigma(FG)/FG)^2 + \sigma(G_0)^2} \quad (4)$$

$$\sigma(G_{BP}) = \sqrt{(-2.5/\ln(10)\sigma(FG_{BP})/FG_{BP})^2 + \sigma(G_{BP_0})^2} \quad (5)$$

$$\sigma(G_{RP}) = \sqrt{(-2.5/\ln(10)\sigma(FG_{RP})/FG_{RP})^2 + \sigma(G_{RP_0})^2} \quad (6)$$

where FG , FG_{BP} and FG_{RP} are the mean fluxes in the G , BP and RP bands, respectively, and $\sigma(G_0) = 0.0027553202$, $\sigma(G_{BP_0}) = 0.0027901700$ and $\sigma(G_{RP_0}) = 0.0037793818$, are the *Gaia* EDR3 zero point uncertainties⁴.

3. Photometric selection of the input sample

In this section, we describe and discuss how we performed the final photometric selection of the sample used as input for the subsequent clustering analysis, that is based on the astrometric and kinematic *Gaia* EDR3 parameters, as will be described in Sect. 4.

By considering the typical complexity of the environment of young stars and the dependence of the reddening law from the stellar effective temperature due to the large spectral range covered by the *Gaia* bands (Anders et al., 2019), we do not attempt to correct colors and magnitudes for reddening and absorption but we use their observed values. This is certainly one of the main source of contamination by older stars that will be overcome as will be discussed later.

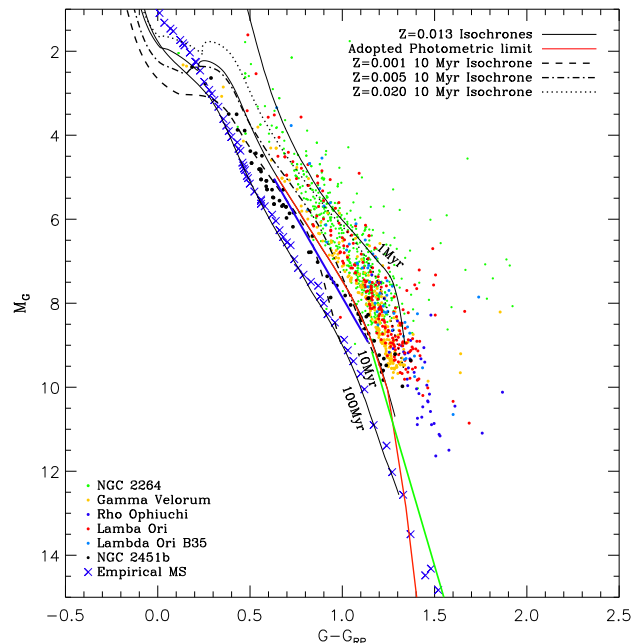


Fig. 1. CAMD of YSOs of some representative young clusters with membership probabilities >0.90 assigned by combining spectroscopic and *Gaia* EDR3 criteria (Jackson et al., 2022). Blue x symbols trace the empirical sequence by Pecaut & Mamajek (2013). Members of the clusters Gamma Velorum (18 Myr old) and NGC2451b (50 Myr old) are also shown. Black solid lines are the theoretical solar metallicity PISA isochrones while the red solid line is the complete photometric limit adopted in this work including the low mass extrapolation. Dashed, dashed-dotted and dotted lines are the 10 Myr isochrones at different metallicities. Blue and green solid lines represent the limits described by the equations 2 and 3.

Our goal is to start from a complete sample, including all potential YSOs with ages < 10 Myr, at least in the photometric range set as described in Sect. 2. In particular, we selected the objects with M_G falling on the red side of the solar metallicity 10 Myr isochrone computed using the PISA models (Dell’Omodarme et al., 2012; Randich et al., 2018; Tognelli et al., 2018, 2020), in the M_G vs. $G - G_{RP}$ diagram shown in Fig. 1. To check if the selected photometric limit is compliant with our requirements, we compared it with the reddening uncorrected CAMD of some SFRs and young clusters for which membership has been recently derived by Jackson et al. (2022), based on the 3D kinematics of the spectroscopic targets. We find that the adopted 10 Myr isochrone delimits the PMS region of clusters, such as NGC 2264, Lambda Ori, Lambda Ori B35 and Rho Ophiuchi, that are in the age range ($t < 10$ Myr) of our main interest. However, also members of ~ 20 Myr old clusters, such as Gamma Velorum, fall completely in the selected photometric region, while members of ~ 50 Myr old clusters, such as NGC 2451b, fall partially in the selected photometric region at $M_G \gtrsim 9$. Going to clusters with ages $t > 50$ Myr the overlapping region occurs at fainter magnitudes.

Since the adopted isochrone is limited to $0.1 M_\odot$, corresponding to $M_G=10.7$, the photometric limit at fainter magnitudes has been extrapolated using a linear extrapolation. To check the position of such extrapolation, we compared it with the empirical sequence by Pecaut & Mamajek (2013) for which mean stellar colors and effective temperatures are given down to $0.1 M_\odot$. The mean stellar colors and effective temperatures can be used as upper limit to the

³ https://gitlab.com/icc-ub/public/gaiadr3_zero_point_bias

⁴ See <https://www.cosmos.esa.int/web/gaia/edr3-passes> and Spectral types and the

region we are interested on. Our photometric limit approaches such sequence and crosses it at $M_G \sim 13$. This ensures us to set an inclusive photometric selection close to the MS at the lowest mass tail. In fact, even though this implies the inclusion of stars older than 10 Myr, on the other hand, it avoids a bias against the selection of very young stars.

We note that for the photometric selection, the minimum and maximum M_G associated to each observed star have been computed by considering the 1σ parallax uncertainties, that are dominating with respect to the magnitude uncertainties. The photometric selection with respect to the reference isochrone has been performed by considering the compatibility of M_G magnitudes, with respect to their minimum and maximum values, i.e. they were selected if either their minimum or maximum value lie inside the selection region. At the end of this selection we remain with a catalogue of 18 057 300 *Gaia* EDR3 entries.

Performing a photometric selection as inclusive as possible, as we have done, implies the introduction of a significant contamination by old field or open cluster stars, mainly due to the uncorrected reddening, binarity or to the overlapping photometric region, at the low mass range, where the sensitivity of the $G - G_{RP}$ colors in distinguishing PMS or MS stars becomes very low.

However, the contamination by field stars does not represent a strong issue for our clustering analysis, since they are not expected to share similar astrometric and kinematic properties. In addition, since we aim at investigating the low mass component of the SFRs, that is also the most dominant ($\geq 80\%$ Lada, 2006), the statistical contrast with respect to field contaminants is expected to be favorable to detect them.

A more tricky effect of our inclusive photometric selection is that also clusters older than 10 Myr can partially fall in the selected region and be recognized as candidate clusters in the subsequent analysis. As shown in Fig. 1, at faint absolute magnitudes ($M_G > 9$), the model-computed isochrones are not very sensitive to stellar ages, and tend to overlap, especially in the M_G vs. $G - G_{RP}$ diagram. In addition, spectral synthesis of M dwarf stars suffers from the accuracy of the adopted atmosphere models and/or from incomplete molecular data. The model-predicted colors of very low mass stars are therefore uncertain. A further complication is the observed discrepancy between radii and colors of low mass stars, likely due to the distorting effects of magnetic activity and starspots on the structure of active stars (Somers et al., 2020; Franciosini et al., 2021). All these effects cause a spread of the low mass MS and can bring magnitudes and colors of ~ 100 Myr old stars to fall in the region selected by us as compatible to stars with $t < 10$ Myr. For all these reasons, as discussed for example in Jeffries et al. (2017), the ages judged from "standard" isochrones are almost certainly underestimated due to a systematic bias.

At faint magnitudes, the fraction of old cluster members falling in the adopted photometric region decreases with cluster ages. Hence clusters of about 20-30 Myrs will be almost completely included in our selected sample, while at the age of 100-500 Myr only the low mass tail will be included. However, because of the adopted photometric limit, the low mass tails will be included only for relatively close clusters ($d < 500$ pc).

As already mentioned before, a partial contamination by old cluster members in our photometric sample can occur also for bright stars ($M_G < 9 - 10$) if their reddening or a binary status gives them observed magnitudes and colors compatible with the selected photometric region. As shown in the Appendix A, the effects of using colors and magnitudes uncorrected for reddening are expected to be more severe for reddened stars with spectral

types earlier than G, in comparison with later spectral types, in the sense that the selected sample is expected to be contaminated mainly by these objects, falling in the brightest part of the photometric region adopted in this work. The implications of this contingency will be discussed in the following sections.

Finally, we also considered the possible effects due to the metallicity on the selection by considering 10 Myr isochrones for metallicity lower or higher than solar. The comparison shows that while YSOs with over solar ($Z=0.020$, $[\text{Fe}/\text{H}]=0.2$) or sub solar ($Z=0.005$, $[\text{Fe}/\text{H}]=-0.45$) metallicities would fall in the selected photometric region, very metal poor YSOs ($Z=0.001$, $[\text{Fe}/\text{H}]=-1.10$) would remain outside. However, as recently found by Spina et al. (2017) at Galactocentric radii from ~ 6.5 kpc to 8.70 kpc, young open clusters and SFRs have close-to-solar or slightly sub-solar metallicities and therefore we conclude that no SFRs are expected to be missed for metallicity effects with our photometric assumptions.

Based on the adopted photometric selection, our data set encompasses substantially all YSOs with age $t \lesssim 10$ Myr and observed $M_G > 5$, including the most reddened ($A_V < 3 - 4$) that can be detected with *Gaia*. Even YSOs with accretion (e.g. Gullbring et al., 1998) or seen in scattered light (Bonito et al., 2013) or flares in M-type stars (e.g. Mitra-Kraev et al., 2005) are expected to be included in our sample. In fact, these phenomena affect the $G_{BP} - G$ or the $G_{BP} - G_{RP}$ colors, causing the stellar colors becoming bluer than their photospheric colors, while, on the contrary, their effect on the $G - G_{RP}$ colors goes in the same direction of the reddening, causing these latter colors to become redder.

We stress, however, that the constraint $M_G < 5$, adopted to strongly reduce the contamination due to reddened Turn-off or MS stars, makes the selected photometric sample incomplete for the massive stellar component of the SFRs. A further expected missing stellar component is that of binary systems of the clusters, due to the restriction of the *Gaia* data to $\text{RUWE} < 1.4$ (see Appendix B). In addition, since available data do not allow us obtaining reliable corrections for the reddening affecting colors and magnitudes of the selected YSOs, accurate stellar parameters such as individual stellar ages and masses will not be derived in the subsequent analysis. However, even though the results we aim to achieve are not suitable for investigations based on complete young populations or accurate stellar parameters, they are expected to trace the dominant component of the SFRs, i.e. their low mass population, and will be crucial to have an overall systematic view of the Galactic SFRs located within 1-2 Kpc from the Sun, as well as for detailed individual or statistical investigations of these YSOs.

4. Method

4.1. Clustering with DBSCAN

This section describes the methodology used to search for candidate clusters with an unsupervised algorithm as overdensities in the five-dimensional (5D) *Gaia* EDR3 astrometric and kinematics parameters ($l, b, \pi, \mu_{\alpha^*}, \mu_{\delta}$).

Starting from the data set selected as described in the Sect. 3, we performed a clustering analysis using the DBSCAN code (Ester et al., 1996), within the scikit-learn machine learning package in Python. First of all, we prepared a grid of $5^\circ \times 5^\circ$ boxes, covering the entire range of the Galactic longitudes l and for $|b| < 30^\circ$. In this step, we took into account the discontinuity at $l = 0^\circ$. To homogenise the variables having different dimensions to comparable values, the five parameters ($l, b, \pi, \mu_{\alpha^*}, \mu_{\delta}$)

within each box were first re-scaled using the `RobustScaler` Python code based on a statistics that is robust to outliers, according to the interquartile range.

The DBSCAN algorithm requires only two input parameters (ϵ , $minPts$). It identifies candidate clusters as overdensities in a multi-dimensional space (5D in our case) in which the number of sources exceeds the required minimum number of points $minPts$, within a neighborhood of a particular linking length ϵ , for all the five parameters, using a statistical distance, assumed to be Euclidean. DBSCAN does not require to know an *a priori* number of clusters and it is able to detect arbitrarily shaped clusters. This is crucial for our analysis aimed to find SFRs that can be characterised by circular or elongated or asymmetric shapes, reminiscent of the native molecular clouds. In order to determine the best input parameters (ϵ , $minPts$) to give as input to DBSCAN, we experimented several values in the direction of well known SFRs and we noted that in the same direction more than a combination of the two parameters is needed to reveal different real clusters located at different distances. This is due to the fact that close candidate clusters, such as associations and co-moving groups, can appear spatially (in l and b) sparse while they are definitively clustered in distance and proper motions, while in the same direction it is possible to identify distant, but spatially concentrated candidate clusters. In the two cases the choice of two different ϵ values rather than a single ϵ is required to detect these kinds of clusters.

Based on this preliminar empirical analysis, we decided to run the DBSCAN codes in the entire Galactic Plane, by adopting a total of 900 combinations of (ϵ , $minPts$) values with ϵ ranging from 0.1 to 9 in steps of 0.1 and $minPts$ ranging from 5 to 50 in steps of 5. In addition, to account for candidate clusters falling in the borders of the defined boxes, we defined another 4 sets of grids, by shifting the original boxes by $\delta l = \delta b = [0.1^\circ, 0.2^\circ, 0.3^\circ, 0.4^\circ]$ with respect to the original boxes. In the following we will refer to the 5 sets of grids as spatial configurations. At the end, we run DBSCAN within a total of $360/5 \times 60/5 \times 5 = 4320$ different boxes with 900 combinations of parameter sets (ϵ , $minPts$).

4.2. Candidate cluster validation

One of the most challenging phases of this analysis has been the validation of the recognized candidate clusters. In fact, DBSCAN is an unsupervised density-based algorithm and, as a consequence, it picks up not only overdensities which correspond to real OCs, but also overdensities only in statistical terms. For this reason, our *a posteriori* validation approach has been based on the exploitation of two astrophysical constraints, based on the typical properties of the SFRs, by avoiding the introduction of strong biases.

SFRs are not characterised by well defined age sequences and they are typically observed in the Hertzsprung-Russell (HR) diagrams as ensemble showing an apparent luminosity spread, often associated to an age spread (e.g. Palla & Stahler, 1999; Palla et al., 2005). On the other hand, such spreads have also been ascribed to complex phenomena affecting their photometry, such as variability, accretion and outflows, extinction, binarity and to our inability to quantify their contribution (Soderblom et al., 2014).

Nevertheless, SFRs are usually observed with a typical mass distribution, that can be shaped by a standard (or closely resembling) Initial Mass Function (IMF), characterised by an increasing fraction of members going towards decreasing masses, at

least until masses of $\sim 0.3M_\odot$ (e.g. Salpeter, 1955; Scalo, 1998; Chabrier, 2003).

Since we are exploiting the excellent *Gaia* EDR3 results down to $G = 20.5$, within reasonable reddening values ($A_V \lesssim 1$), with our data set, we expect to detect YSOs with spectral type down to M-type, at distance $\lesssim 1.5$ kpc. This is the case, for example, of the cluster NGC 6530, located at around 1.3 kpc, for which the low mass population down to $0.4M_\odot$ has been detected at $V \sim 20$ (Prisinzano et al., 2005), roughly corresponding to our G magnitude limit.

Based on these considerations a physical recognisable candidate cluster should include its tail of low mass members. Hence, we imposed a minimum threshold of 10 objects with $M_G > 7.7$, that means to require candidate clusters having at least 10 stars with $M \lesssim 0.5M_\odot$, assuming the isochrone of 10 Myr from the Pisa models.

A further parameter that we considered as an indicator of reliability for the candidate cluster validation is the dispersion of the distances of each cluster. The observed total distance dispersion is a combination of the intrinsic dispersion plus the contribution due to the measurement errors. While the intrinsic dispersion does not depend on the distance, the contribution due to the measurement errors becomes dominant at large distances, since *Gaia* EDR3 parallaxes become much more uncertain. Thus, among the parameters used to find over-densities by DBSCAN, the observed standard deviation of the distances is the most critical parameter to be constrained for the identification of real clusters. To this aim, for the cluster validation, we constrained the maximum allowed observed dispersion. For distances < 1 kpc, the constrain is set on the ratio between the standard deviation of the distances of the putative members and the derived mean distance for the given candidate cluster. For a valid candidate cluster the above ratio has to be < 0.2 . For more distant candidate clusters, we adopted the more stringent constrain that the standard deviation should be smaller than 200 pc. This limit has been chosen by considering that for NGC 2244 located at ~ 1.6 Kpc, one of the most distant clusters that we detect, the distance dispersion is about 175 pc and therefore we do not expect to find physical real clusters with a distance dispersion larger than this threshold. These choices may limit our ability to detect clusters at distance $\gtrsim 1.5$ kpc for which we could, in principle, detect, at the magnitude limit of our data set, the massive component of the clusters down to $\sim 1M_\odot$ regime. However, since the accuracy of *Gaia* EDR3 parallaxes and kinematic data beyond this limit becomes very low, we prefer to maintain our constraints at the price of limiting our analysis to smaller distances.

The adopted constrains on the distance dispersion of cluster members have shown to be very effective in rejecting a large number of (unexpected) candidate massive clusters recognized by DBSCAN, typically with more than ~ 1000 members, located at distances $\gtrsim 1$ Kpc, that do not include M-type stars, but only earlier stars and that are characterised by very large dispersions in distance. These structures are likely those identified as strings in Kounkel & Covey (2019); Kounkel et al. (2020). However, since we do not recognise these structures as standard clusters, any further investigation of them is beyond the scope of this work.

The final cluster member selection has been performed only for candidate clusters that satisfy the previous constraints. As a result of our choice of the DBSCAN input parameters (see Sect. 4.1) and of the adopted spatial configurations, a given candidate cluster can be identified by adopting similar input parameters, with possible small differences in the cluster membership.

In addition, a given candidate cluster can be identified in more than one box, with the same membership result, if the candidate cluster is spatially small enough to be completely identified, for a given couple of input parameters, in two or more overlapping boxes. Alternatively, it can be completely detected within one box and only partially detected in a box where the candidate cluster falls at the borders. In order to assign the most likely membership for a given cluster, we proceeded adopting the following strategy.

We first considered the candidate clusters detected within the same spatial configuration but with different set of parameters (ϵ , $minPis$). For each of the selected candidate clusters, we computed the median values of the 5 parameters (l , b , π , μ_{α^*} , μ_{δ}) and then we selected all the candidate clusters that were simultaneously compatible in these 5 parameters i.e. if the two compared distributions of each parameter overlap around the median, within half of the total width. Among the compatible candidate clusters, we selected the most populated and discarded the others. This strategy allowed us to identify the most persistent candidate clusters at different scales.

In the subsequent step, we compared the candidate clusters identified in each of the five spatial configurations to select the *best* configuration, or likewise, the *best* box in which the spatial coverage of the candidate cluster is maximised. Since we can have more than one detection of the same cluster, for each member, we selected only the configuration in which it is associated to the most populated candidate cluster and that member was removed from the less populated clusters in which it was identified by DBSCAN. The peripheral members of candidate clusters covering a spatial region larger than the area of the box ($5^\circ \times 5^\circ$), left out from the richest centered candidate cluster, were considered as additional candidate clusters only if they include at least 10 elements,⁵ as also assumed in other similar works, (e.g. Castro-Ginard et al., 2018; Kerr et al., 2021). This selection strategy allowed us to include also likely members at the candidate cluster's periphery, providing data for further investigations on the dynamics of these stellar clusters. At the end of this process, we are left with a total of 449 849 detected stars within 14 178 single candidate clusters.

Many SFRs are associated to giant molecular clouds and thus they can have a spatial extension larger than the box of $5^\circ \times 5^\circ$ used for our analysis. In order to merge candidate clusters belonging to the same complex, we proceeded as follows: we computed the median and the 16% and 84% percentiles of the distance and proper motion distributions. Then, we merged all neighboring clusters for which distances and proper motions were compatible within 1σ . The total number of merged clusters is 7 323.

4.3. Cluster age classification

From a visual inspection of the photometric properties of the clusters found with this analysis, we noted that, while, as expected, for most of the recognized clusters their selected members of any mass stay in the PMS region of the CAMD, there is a fraction of recognized clusters for which only the low mass members stay in that PMS region. This is, for example, the case of clusters with low or moderate extinction ($A_V \lesssim 1$) and age $10 \text{ Myr} \lesssim t \lesssim 50 \text{ Myr}$ such as IC 2602, Melotte 20, NGC 2451 A, NGC 2451 B, where part of the MS or PMS low mass tail ($M_G \gtrsim 9$) overlaps the photometric region considered here. For clus-

ters with ages $t \sim 100\text{-}200 \text{ Myr}$, such as for example Melotte 22 (Pleiades), NGC 2422, NGC 2516 a smaller fraction of the MS low mass tail, likely composed by reddened members, cluster binaries or PMS members, is selected.

Further reddening effects or poorly constrained magnitudes or parallaxes, can bring colors or magnitudes of members of even older clusters within the PMS photometric region considered in this work. For clusters with extinction $A_V \gtrsim 1$, the MS of $t \gtrsim 100 \text{ Myr}$ old clusters in the range $5 < M_G \lesssim 8$ fall to the right of the unreddened 10 Myr isochrone. Thus, depending on the cluster age, binaries or reddened members of clusters with ages $t > 10 \text{ Myr}$ can also fall in the selected photometric region. Since these objects share the same proper motions and are at the same distance, they are recognized as belonging to a cluster and are therefore included in our catalogue.

To distinguish SFRs from old clusters, we adopted a pattern match procedure based on the extraction of the different patterns that characterise the observed CAMD of clusters of different ages. Among the clusters identified as described in the previous sections, we selected those listed in Table 1 (52 in total) and we used them as template data set.

In the template data set, we identified 28 clusters, shown in Fig. 2, that have been used by us as proxy for clusters with ages $t \lesssim 10 \text{ Myr}$. Such clusters were selected since most of them show a consistent luminosity spread, typical of the SFRs, starting from our brightest limit $M_G=5$. However, their general shape is also set by the reddening and the distance, with the observed M_G maximum limit that increases as distance decreases. All these cases have been included in the template data set to retrieve all the possible patterns observed in the CAMD due to different ages, distances, reddening and cluster richness. For each of these clusters, we assigned an increasing flag from 1 to 28, aimed to represent the different shapes of the observed CAMD shown in Fig. 2.

We identified also 8 clusters as representative for the ages $10 \lesssim t/\text{Myr} \lesssim 100$, flagged from 29 to 36, according to the ages given in Cantat-Gaudin & Anders (2020). The observed CAMD of these clusters are shown in Fig. 3. These clusters show an evident PMS region that is mainly populated in the range $M_G \gtrsim 8$ (e.g. NGC 2451B, NGC 2232), due to our photometric selection. Such region becomes thinner and thinner for older clusters such as Melotte 20 and Melotte 22. Finally, we selected 16 clusters, flagged from 37 to 52, as proxy for clusters with ages $t \gtrsim 100 \text{ Myr}$, in agreement with Cantat-Gaudin & Anders (2020). Most of these clusters have been included in the template sample to take into account the non-uniform distribution of the absolute magnitudes of their members in the observed CAMD. In fact, while for very young clusters it is uniformly populated, accordingly to their age and the IMF, for these reddened and old clusters, the population is not entirely identified. For example, the clusters with flag from 43 to 52 are characterised in the CAMD by an overdensity of members with $M_G \lesssim 9$. Most of them are quite distant clusters ($d \gtrsim 500 \text{ pc}$) and thus very likely affected by reddening. As shown in Appendix A, the effect of the reddening for the Gaia bands, depends on the stellar effective temperature (Anders et al., 2019), and for high mass stars such effect is larger than for low mass stars. This would explain the presence of the peak at higher masses in the observed magnitudes of the CAMD for most of these clusters. Depending on the cluster distance, also part of the low mass tail is detected, but the overall non-uniform pattern of their CAMD is different from that expected for young clusters.

Since most of the clusters show asymmetric structures, to evaluate their extension we estimated the radius in which

⁵ For this reason, our catalogue includes cases in which a single physical cluster is identified by more than one DBSCAN cluster.

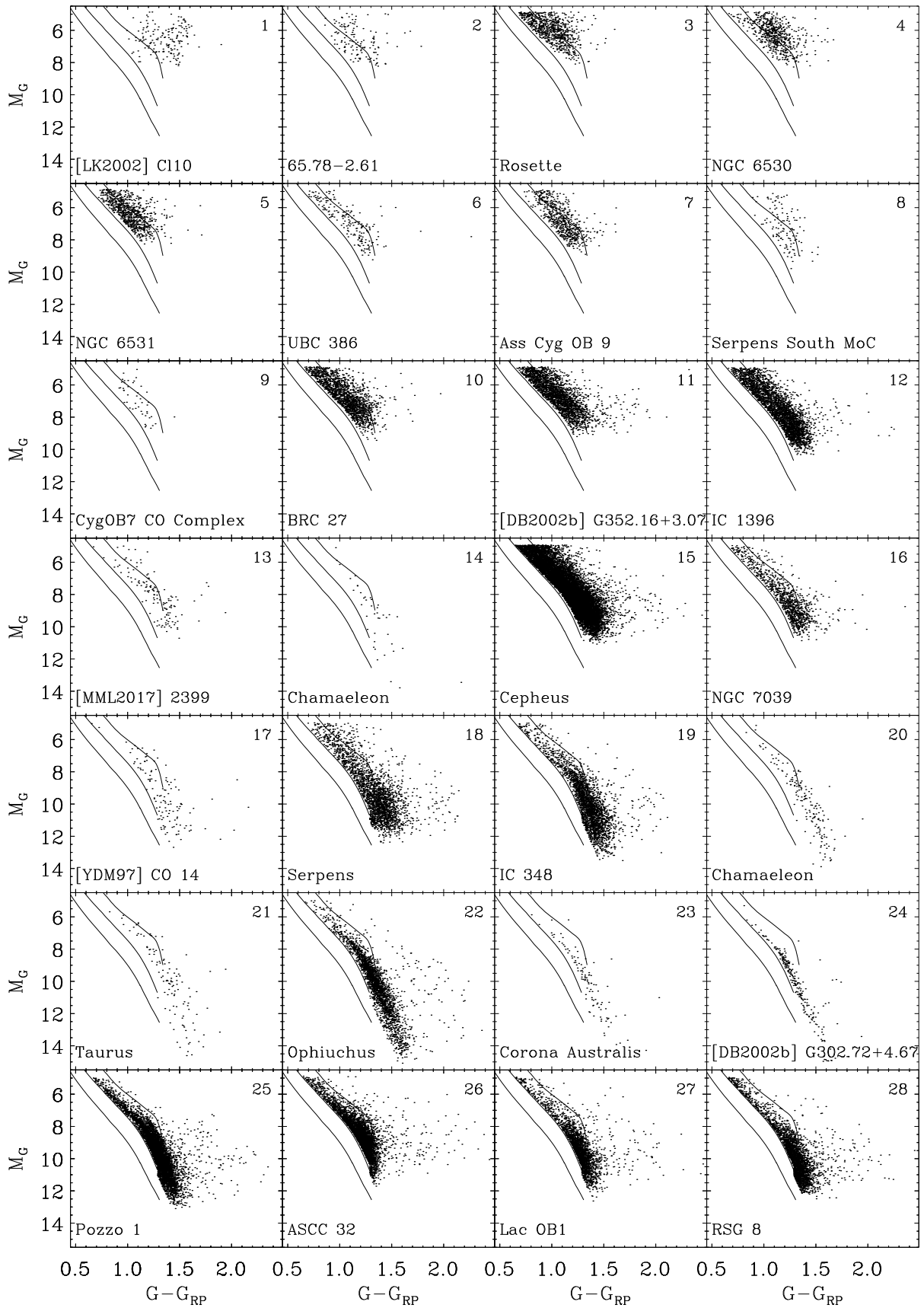


Fig. 2. CAMD of YSOs identified in the clusters with ages $t \lesssim 10$ Myr included in the template data set. Black solid lines are the theoretical solar metallicity Pisa isochrones of 1, 10 and 100 Myr isochrones (from right to left). The number on the top right edge of each panel is the flag assigned to each cluster.

Table 1. Clusters used as template data set to select SFRs and other stellar clusters. Flag is the value assigned to each cluster to characterise a given observed CAMD shape. r_{50} is the radius in which half of the identified members are concentrated, d is the distance obtained by inverting the median value of the member parallaxes and N is the number of members.

Literature Name	Flag	Reference	l [deg]	b [deg]	r_{50} [deg]	d [pc]	$\log t$ [yr]	N
[LK2002]C110	1	Le Duigou & Knödseder (2002)	79.867	-0.908	0.886	1557		167
65.78-2.61	2	Avedisova (2002)	66.153	-3.123	1.194	1324		134
Rosette	3	Zucker et al. (2020)	206.438	-1.903	2.025	1571	7.1	810
NGC 6530	4	Dias et al. (2002)	6.060	-1.287	1.020	1364		635
NGC 6531	5	Dias et al. (2002)	7.585	-0.338	1.634	1350	8.6	804
UBC 386	6	Cantat-Gaudin & Anders (2020)	100.562	8.694	1.147	1280	6.8	193
Ass Cyg OB 9	7	Sitnik (2003)	78.753	1.778	2.293	1339	8.1	616
Serpens South molecular cloud	8	Fernández-López et al. (2014)	29.364	2.870	0.976	920		123
CygOB7 CO Complex	9	Dutra & Bica (2002)	92.653	2.529	0.950	1123		46
BRC 27	10	Rebull et al. (2013)	224.621	-2.244	3.027	1233	6.9	1709
[DB2002b] G352.16+3.07	11	Otrupcek et al. (2000)	-7.866	3.002	4.764	1169	7.0	2357
IC 1396	12	Zucker et al. (2020)	99.236	4.733	7.407	945	7.4	3140
[MML2017] 2399	13	Miville-Deschênes et al. (2017)	33.890	0.643	2.543	609		130
Chamaeleon II	14	Zucker et al. (2020)	-56.363	-14.720	2.452	200		41
Cepheus	15	Zucker et al. (2020)	108.911	4.359	9.748	923	8.2	11445
NGC 7039	16	Cantat-Gaudin & Anders (2020)	88.350	-1.717	5.322	767	7.3	1048
[YDM97] CO 14	17	Yonekura et al. (1997)	104.508	13.950	3.039	350		124
Serpens	18	Zucker et al. (2020)	28.783	3.082	10.166	455	7.2	2388
IC 348	19	Cantat-Gaudin & Anders (2020)	160.790	-15.812	11.430	334	7.4	2661
Chamaeleon I	20	Zucker et al. (2020)	-62.781	-15.444	3.099	192		156
Taurus	21	Zucker et al. (2020)	172.114	-15.302	4.551	131		112
Ophiuchus	22	Zucker et al. (2020)	-8.024	18.781	12.655	144		2398
Corona Australis	23	Zucker et al. (2020)	-0.132	-17.592	3.291	155		107
[DB2002b] G302.72+4.67	24	Dutra & Bica (2002)	-57.143	4.739	5.854	112		235
Pozzo 1	25	Cantat-Gaudin & Anders (2020)	261.858	-8.321	13.343	398	8.3	6001
ASCC 32	26	Cantat-Gaudin & Anders (2020)	237.327	-9.186	9.878	818	8.4	4416
Lac OB1	27	Chen & Lee (2008)	96.762	-15.032	11.268	548	7.4	2367
RSG 8	28	Cantat-Gaudin & Anders (2020)	109.331	-1.212	12.055	468	7.4	2900
NGC 2451B	29	Cantat-Gaudin & Anders (2020)	253.198	-7.499	9.513	401	7.6	2826
NGC 2232	30	Cantat-Gaudin & Anders (2020)	215.533	-7.983	13.427	372	7.2	1703
Sco OB2 UCL	31	de Zeeuw et al. (1999)	-29.000	16.813	15.052	145		1189
IC 2602	32	Cantat-Gaudin & Anders (2020)	-70.259	-5.011	6.825	151	7.6	315
NGC 2516	33	Cantat-Gaudin & Anders (2020)	-86.236	-15.931	6.881	427	7.6	1156
Melotte 20	34	Cantat-Gaudin & Anders (2020)	147.504	-6.461	8.867	174	7.7	414
Melotte 22	35	Cantat-Gaudin & Anders (2020)	166.573	-23.406	5.882	137	7.9	296
NGC 2422	36	Cantat-Gaudin & Anders (2020)	230.995	3.061	6.238	500	8.0	347
Alessi 12	37	Cantat-Gaudin & Anders (2020)	67.678	-11.723	3.977	546	8.1	127
NGC 3532	38	Cantat-Gaudin & Anders (2020)	-72.815	2.279	4.851	561	8.6	88
IC 6451	39	Cantat-Gaudin & Anders (2020)	-19.939	-7.821	1.257	1068	9.2	86
NGC 6087	40	Cantat-Gaudin & Anders (2020)	-32.077	-5.426	2.532	1007	8.0	77
Alessi 62	41	Cantat-Gaudin & Anders (2020)	53.676	8.773	3.561	622	8.4	87
UPK 33	42	Cantat-Gaudin & Anders (2020)	27.965	0.108	3.931	518	8.4	111
NGC 1647	43	Cantat-Gaudin & Anders (2020)	180.355	-16.861	2.141	606	8.6	272
NGC 6124	44	Cantat-Gaudin & Anders (2020)	-19.205	6.078	5.404	648	8.3	1102
NGC 6494	45	Cantat-Gaudin & Anders (2020)	9.714	2.980	5.537	755	8.6	680
IC 4725	46	Cantat-Gaudin & Anders (2020)	14.022	-4.595	4.807	669	8.1	788
Alessi 44	47	Cantat-Gaudin & Anders (2020)	37.075	-11.510	7.285	587	8.2	637
Stock 2	48	Cantat-Gaudin & Anders (2020)	133.371	-1.160	8.292	384	8.6	727
NGC 2168	49	Cantat-Gaudin & Anders (2020)	186.647	2.327	2.616	928	8.2	118
DSHJ2320.1+5821A	50	Kronberger et al. (2006)	111.248	-2.785	2.394	1131		243
UPK 143	51	Cantat-Gaudin & Anders (2020)	91.810	0.514	1.752	934	8.4	262
Collinder 421	52	Cantat-Gaudin & Anders (2020)	79.429	2.527	1.061	1265	8.4	154

Notes. Flag=[1, 28] are assigned to clusters with ages $t \leq 10$ Myr, Flag=[29, 36] are assigned to clusters with ages $10 \leq t/\text{Myr} \leq 100$, Flag=[37,52] are assigned to clusters with ages $t \geq 100$ Myr.

half of the identified members are concentrated, as $r_{50} = 0.5 \times \sqrt{(\text{width}^2 + \text{height}^2)}$, as done in Cantat-Gaudin & Anders (2020).

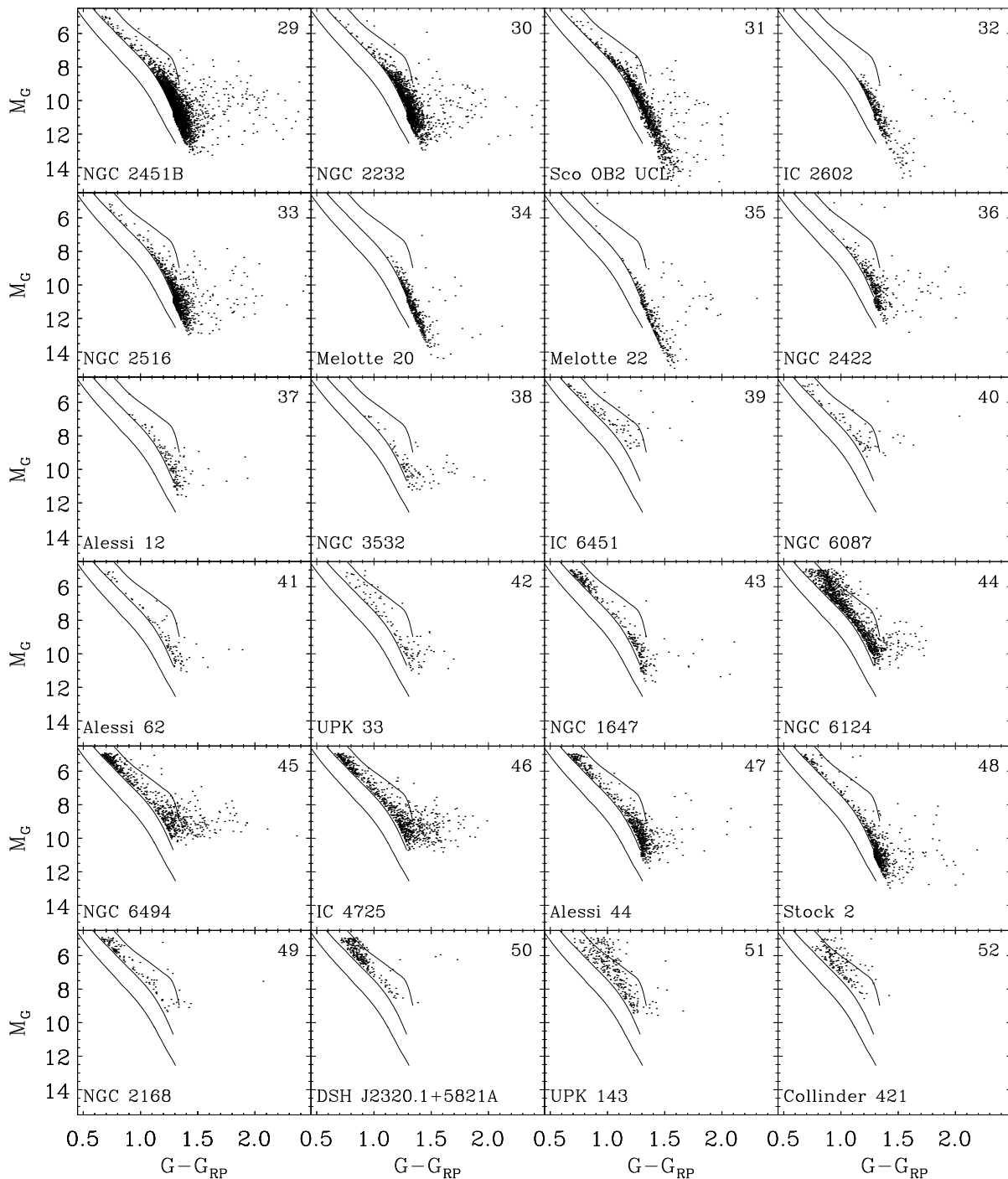


Fig. 3. CAMD of clusters with ages $10 \text{ Myr} \leq t \leq 100 \text{ Myr}$, flagged from 29 to 36, and with ages $t \geq 100 \text{ Myr}$, flagged from 37 to 52, included in the template data set. Black solid lines are as in Fig. 2. The number on the top right edge of each panel is the flag assigned to the clusters.

In our final catalogue, we also noted the presence of other photometrically unphysical aggregates including mostly only faint stars (with $G > 18.5$), with very red $G - G_{RP}$ colors, with an horizontal distribution in the CAMD, likely compatible with those of giant stars and with M_G nearly constant. Since most of these peculiar clusters are in the direction of the Galactic

Centre, we infer that they correspond to very distant giants for which *Gaia* EDR3 parallaxes are systematically wrong due to the strong effects of crowding and high extinction in the direction of the Galactic Center.

To separate these aggregates from SFRs or stellar clusters, we included in our template data set further 27 cases of these pec-

cular aggregates, flagged from -27 to -1, with median M_G from 7.6 to 15.8, covering their observed magnitude values.

According to the known ages of the clusters of the template data set, we defined the three age bins, $t \leq 10$ Myr, $10 \leq t/\text{Myr} \leq 100$ and $t \geq 100$ Myr, including the clusters with flags in the ranges [1, 28], [29, 36] and [37, 52], respectively. Then we used a python implementation of the two-dimensional version of the Kolmogorov-Smirnov (KS) test⁶, developed by Peacock (1983) and generalised by Fasano & Franceschini (1987), to identify for each of the 7323 clusters, the most similar amongst the chosen template clusters in the CAMD, i.e. the one for which the KS statistic is minimum.

The procedure does not intend to derive any best fitting parameter but it is aiming only to assign a flag to each cluster and then a "coarse" age range to which it belongs to. At the end, we selected only the 1450 clusters with more than 20 members (corresponding to 302730 objects), for which the KS test statistic is < 0.2 .

In conclusion, we classified 124440 candidate YSOs that belong to 354 structures with $t \leq 10$ Myr, distributed within ≤ 1.5 Kpc. From now on we will indicate these structures as SFRs, meaning regions that can include at least one very young cluster and mostly consistent of YSOs with $t \leq 10$ Myr. In addition, we classified 65863 low mass members of 322 stellar clusters, mainly located within ~ 500 pc and ages $10 \text{ Myr} \leq t \leq 100$ Myr, and, finally, 43936 members of 524 clusters with $t \geq 100$ Myr. The objects that belong to photometrically unphysical aggregates are 68491. The results are summarised in Tab. 2. From our catalogue we reject all clusters with ages $t \geq 100$ Myr, the photometrically unphysical aggregates and those that remain unclassified since are mainly poorly populated with a CAMD that does not allow to properly classify them.

Table 2. Results of the cluster age classification

Classification	# Stars	# clusters	Flag
$t \leq 10$ Myr	124440	354	[1, 28]
$10 \leq t/\text{Myr} \leq 100$	65863	322	[29, 36]
$t \geq 100$ Myr	43936	524	[37, 52]
Phot. unphysical aggregates	68491	250	[-27, -1]
Unclassified	147119	5887	

SFRs and stellar clusters with ages $t \leq 100$ Myr are listed in Tab. 3, while cluster members are given in Tab. 4. Most of the clusters listed in the table are very extended complex regions including several subclusters known in the literature, merged here within single structures. Since the aim here is to detect these Galactic young structures, the literature cluster names given in Tab. 3, mainly taken from Cantat-Gaudin & Anders (2020) or Zucker et al. (2020) or from Simbad, are only indicative of the region.

5. Results

5.1. Photometric completeness

Within the magnitude range explored in this work and assuming the restrictions on *Gaia* data defined in Sect. 2, the photometric cluster completeness, for clusters with $t \leq 10$ Myr, is expected to be near 100% for not embedded YSOs, since, as shown in Fig. 1, all members detectable in this age range and in the optical bands, are expected to lie in the selected photometric region.

⁶ available at <https://github.com/syrte/ndtest>

Nevertheless, the adopted restriction $RUWE < 1.4$ introduced a bias in the selection of multiple members in the SFRs. To estimate the fraction of missed binary members with the *Gaia*-based selection used in this paper, we used as reference the Tau-Aur binary-star list by Kraus et al. (2012). Details about the comparison of this list with our catalogue and *Gaia* EDR3 data are given in Appendix B. This comparison shows that, due to the $RUWE$ restriction, in SFRs at distances similar to Tau-Aur, we have lost about 72% of their binary populations. Assuming a binary frequency of $\sim 50\%$ (Mathieu, 1994), a loss of $\sim 35\%$ of PMS members can be expected. However, at large distances, the projected binary motions become smaller, and therefore we expect a less significant binary member loss for the farther-out SFRs.

For clusters with ages $t \geq 10$ Myr, the cluster completeness decreases with ages and strongly depends on the cluster distance. In fact, clusters with $10 \text{ Myr} \leq t \leq 100$ Myr (indexed from 29 to 36), are mainly in the solar neighborhood ($d < 500$ pc). For these clusters, even though we are not able to detect the entire cluster population, we are, however, able to detect part of the very low mass tail component. The fraction of the detected very low mass tail component decreases with age and, in fact, for clusters with $t \geq 100$ Myr (indexed from 37 to 52), mainly concentrated at $d \geq 500$ pc, the completeness is very low. These latter have been discarded from our final catalogue since they include only a small fraction of the cluster members and are not in the age range of interest for this work. Clusters with ages $10 \text{ Myr} \leq t \leq 100$ Myr have been included in our catalogue, since the age transition to the clusters with $t \leq 10$ Myr is not sharply defined and, in addition, there are structures such as Sco OB2 that include clusters in both age ranges, that very likely belong to correlated star forming processes.

5.2. Spatial distribution

Figure 4 shows the maps of the 124440 YSOs associated to the 354 SFRs with ages $t \leq 10$ Myr, while Fig. 5 shows the maps of the 65863 stars associated to the stellar clusters with ages $10 \text{ Myr} \leq t \leq 100$ Myr. Each map has been obtained as two-dimensional histogram smoothed with a Gaussian kernel at 3σ , adopting a pixel size of $3 \text{ pc} \times 3 \text{ pc}$.

Most of the overdensities in Fig. 4 are associated to known SFRs, some of which are labeled in the figure. With the exception of those within 200-300 pc, all clusters present a radial elongated shape, tracing the increasing uncertainties in the distances.

The clusters with ages $10 \text{ Myr} \leq t \leq 100$ Myr are mainly limited within ~ 600 pc (see Fig. 5) and show a much more diffuse spatial distribution. Very rich clusters such as, for example, NGC 2232, NGC 2451B, Gamma Velorum, NGC 2547, NGC 2516, Alessi 5 at distance of ~ 400 pc, seem to belong to a common giant complex, mostly lying in the third Galactic quadrant.

5.3. Literature comparison

In this section, we present the comparison of our results with those previously obtained in the literature for two particular regions, Sco OB2 and NGC 2264. These comparisons will be used to estimate our completeness and the contamination level, at least when the completeness of the comparison sample enable us to do it. We note that we will consider here each of the merged clusters as a unique ensemble. A detailed subclustering analysis of them, with the identification of possible substructures with

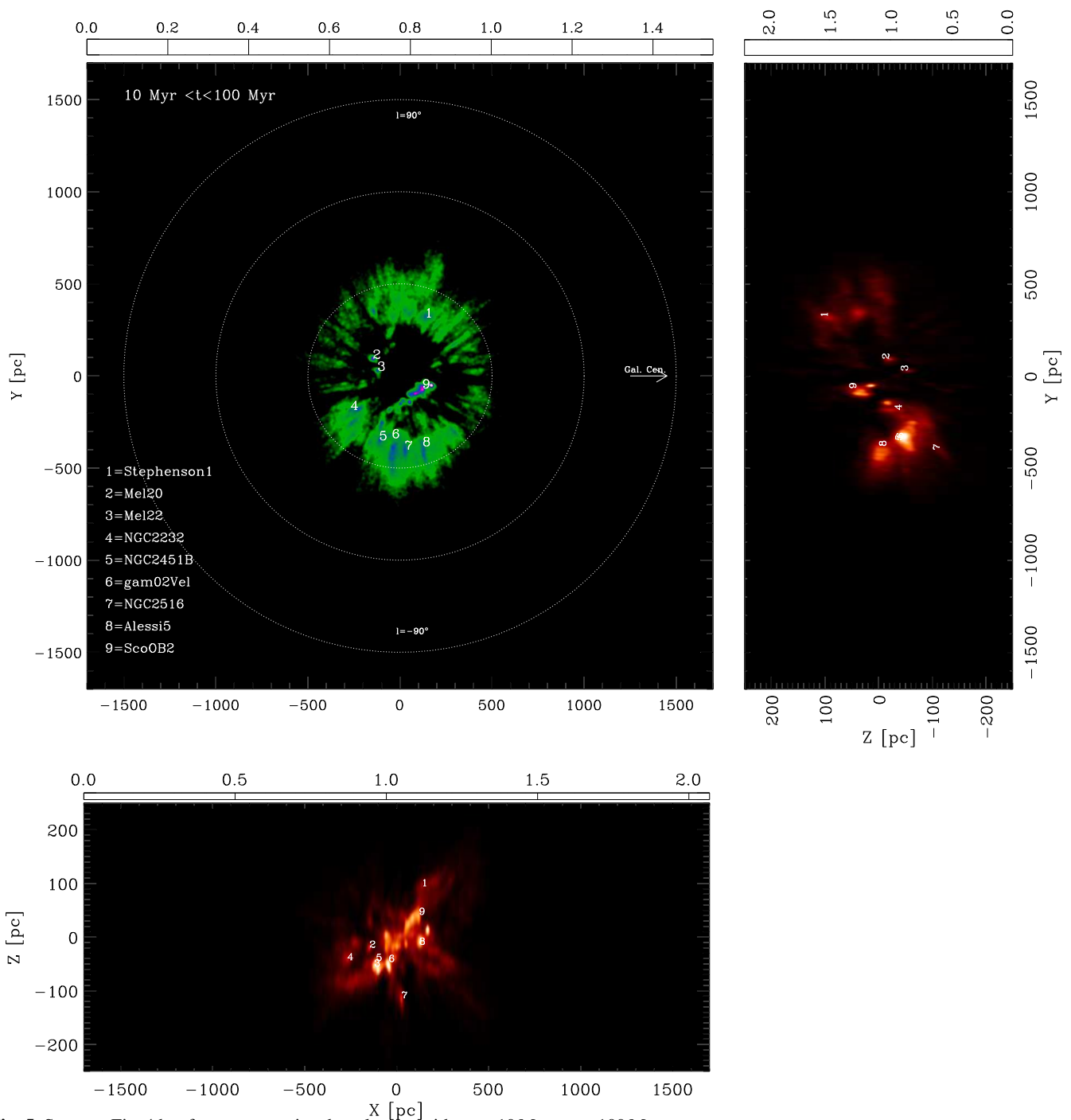


Fig. 5. Same as Fig. 4 but for stars associated to clusters with ages $10 \text{ Myr} \leq t \leq 100 \text{ Myr}$.

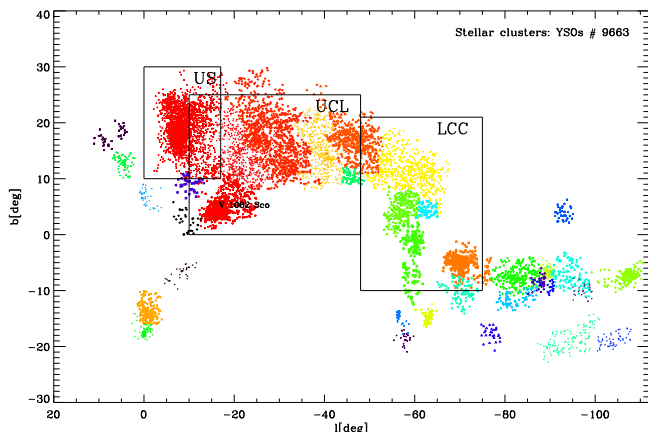
To select the members of this region, we performed a spatial selection by considering all stars with $-102^\circ < l < 10^\circ$, $-30^\circ < b < 40^\circ$ and, as assumed in Damiani et al. (2019), distance $d < 200 \text{ pc}$. We end up with a total of 9 663 YSOs with ages $t \leq 100 \text{ Myr}$, distributed as in Fig. 6. In the (l, b) plane, the pattern of the YSOs associated to Sco-OB2 is that already found in the literature (e.g. de Zeeuw et al., 1999; Damiani et al., 2019; Kerr et al., 2021). Among the selected objects, 4 232 YSOs have been classified in the range $t < 10 \text{ Myr}$. Those concentrated in the Upper Sco (US) region are 2 472. They correspond to the youngest subpopulation of Rho Ophiuchi. Another prominent subpopulation, classified in the range $10 \text{ Myr} \leq t \leq 100 \text{ Myr}$ (flag 31), includes 3 741 YSOs, falling in the Upper Centaurus-Lupus

(UCL) and Lower Centaurus-Crux (LCC) regions. It then represents the first generation of stars of the Sco OB2 region, in agreement with recent results (e.g. Damiani et al., 2019; Luhman, 2022).

Proper motions, parallaxes and the CAMDs of the different subpopulations detected in the Sco OB2 association are shown in Fig. 7. The proper motions of the YSOs associated to Sco-OB2 show a quite complicated pattern, confirming the complex kinematic structure of this association. The values of parallaxes of YSOs in Sco-OB2 are mostly enclosed between $\sim 5 \text{ mas}$ and $\sim 10 \text{ mas}$, corresponding to a mean distance of 152 pc and standard deviation $\sigma = 28 \text{ pc}$. Finally, in the CAMD, we can recognise a usual distribution of YSOs in the PMS region. As already

Table 4. *Gaia* EDR3 data of members of SFRs with $t \lesssim 10$ Myr (flag from 1 to 28) and young stellar clusters with $10 \text{ Myr} \lesssim t \lesssim 100$ Myr (flag from 29 to 36) found in this work. The full table is available as an electronic table via the CDS.

Gaia EDR3 ID	l	b	π	σ_π	μ_α^*	$\sigma_{\mu_\alpha^*}$	μ_δ	σ_{μ_δ}	G	G_{BP}	G_{RP}	Flag	Cl. ID
	[deg]	[deg]	[mas]	[mas]	[mas yr ⁻¹]	[mag]	[mag]	[mag]					
5307477283092480512	276.491	-2.559	1.925	0.071	-13.112	0.093	8.232	0.079	17.27	18.56	16.13	30	1
5310444177789318784	275.554	-3.171	1.923	0.265	-12.888	0.288	8.518	0.327	19.40	20.85	18.02	30	1
5310482871168676352	276.316	-2.671	1.846	0.036	-14.232	0.044	8.038	0.039	16.31	17.24	15.27	30	1
5310525477245693696	275.730	-2.877	1.901	0.030	-12.997	0.034	8.875	0.029	15.63	16.57	14.66	30	1
5310539800934356736	275.547	-2.870	2.004	0.163	-13.991	0.195	9.334	0.171	18.70	20.58	17.38	30	1

**Fig. 6.** Spatial distributions in Galactic coordinates of the YSOs associated to the Sco-OB2 Association. The de Zeeuw et al. (1999) subregions of Upper Sco (US), Upper Centaurus-Lupus (UCL) and Lower Centaurus-Crux (LCC) are shown. The different colors indicate all the different substructures found in this region.

noted, the census of stars that belong to the first generation of stars in the Sco OB2 association is likely incomplete since it is expected to lie in the region of the CAMD that has not been considered in this work.

To estimate the completeness level of our census, we compared our list of Sco-OB2 YSOs with the ones recently published by Damiani et al. (2019) and Kerr et al. (2021), based on *Gaia* DR2 data and by Luhman (2022), based on *Gaia* EDR3 data. To perform these comparisons we used the Gaia identification number of YSOs in our catalogue, retrieved as described in Sect. C.4. We find that the YSOs in common with the Damiani et al. (2019) catalogue, that includes a total 10 839 members, are 6 492. i.e. about 60% of the Damiani et al. (2019) list. Among the 9 663 YSOs selected by us in the Sco-OB2 association, those falling in the spatial region and magnitude range $G < 19.5$ covered by Damiani et al. (2019) are 7 553. Therefore, the objects in common are 86% of our sample in the same field. Many of the remaining 1 061 YSOs (14%) not selected by Damiani et al. (2019) show a spatial distribution consistent with that of the other members and thus we discard the hypothesis that they are contaminants, and suggest that they are likely YSOs missed by Damiani et al. (2019), that is based on the less complete *Gaia* DR2 catalogue.

Adopting the same spatial constraints, we retrieved in the Sco-OB2 region 9 083 objects, selected as candidate YSOs in the Kerr et al. (2021) catalogue, independently from their clustering type of classification. Among these, 5 203 are in common with

our catalogue but those classified as YSOs are 5 109 i.e. $\sim 56.2\%$ of the Kerr et al. (2021) sample⁷.

The Luhman (2022) catalogue includes a total of 10 509 YSOs but to be consistent with our selection, we selected those with $M_G > 5$, $7.5 < G < 20.5$, $R_{UWE} < 1.4$ that are in total 7 925. Using the *Gaia* EDR3 id, we found that the YSOs in common with our catalogue are 6 341 representing 80% of the Luhman (2022) catalogue and 85.6% of our list of YSOs in the Sco Cen, by considering the 7 408 counterparts falling in the region covered by Luhman (2022).

These percentages can not be strictly used to estimate our level of completeness or contamination, since the catalogues have been obtained starting from different initial constraints, both for the photometric and the astrometric selection, that inevitably can introduce several biases. However, these comparisons are useful to confirm the membership for $\sim 85\%$ of the selected members. The remaining 1 067 objects not retrieved by Luhman (2022) but selected by us as YSOs show a spatial distribution consistent with that of the other members with two strong concentrations of them in the US region and around V 1062 Sco. We therefore conclude that they are genuine members rather than contaminants, likely missed by Luhman (2022) in the photometric selection based on the $G_{BP} - G_{RP}$ colors.

5.3.2. The Monoceros OB1/NGC 2264 complex and the Rosette Nebulas

Another well studied region that we used to test our results is the cluster NGC 2264 in the Monoceros OB1 complex. This relatively compact and close (~ 720 pc from the Sun) SFR, devoid of background and foreground emission, has been the subject of many detailed studies, including, for example, X-ray observations (Flaccomio et al., 2006), optical and near IR analysis of its low mass population (Venuti et al., 2019), coordinated synoptic investigations with Optical and Infrared light curves with CoRot and Spitzer (Cody et al., 2014). Flaccomio et al. (2022, in preparation) compiled the most complete data set of NGC 2264, based both on all-sky surveys (*Gaia* EDR3, 2MASS, VPHAS) and dedicated observations falling in the region $98.93^\circ < RA < 101.47^\circ$ and $8.45^\circ < Dec < 10.95^\circ$. The young structure identified by us in this field includes a total of 1 916 YSOs, but only 1 062 of them ($\sim 55\%$) fall in the region investigated by Flaccomio et al. (2022, in preparation). The remaining YSOs are in part (404 YSOs) concentrated in the region corresponding to the cluster IC 446, while a further unknown group of 450 YSOs are sparsely distributed in the Southern region of NGC 2264. As shown in Fig. 8, a sub-group of these latter form a visual bridge along a filamentary structure, clearly visible in the IR IRIS image, down to the loca-

⁷ Using the *Gaia* DR2 number, we cross-matched the Kerr et al. (2021) and Damiani et al. (2019) lists and found 6 423 objects in common.

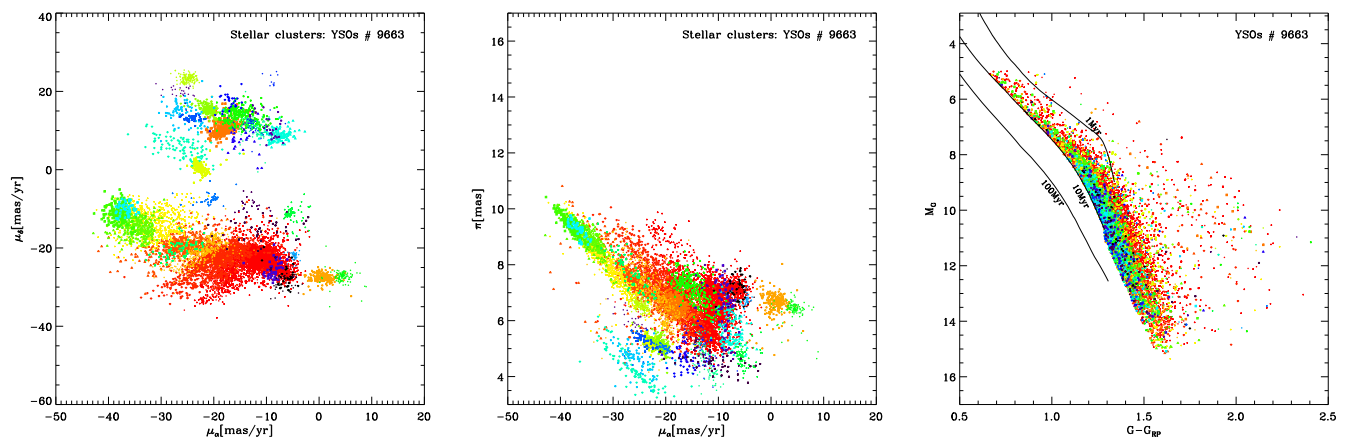


Fig. 7. Proper motions in RA and Dec, parallaxes and CAMDs of the groups of YSOs associated to the Sco OB2 association. The symbol colors are as in Fig. 6. Three representative solar metallicity isochrones from the Pisa models are also shown as solid lines in the right panels.

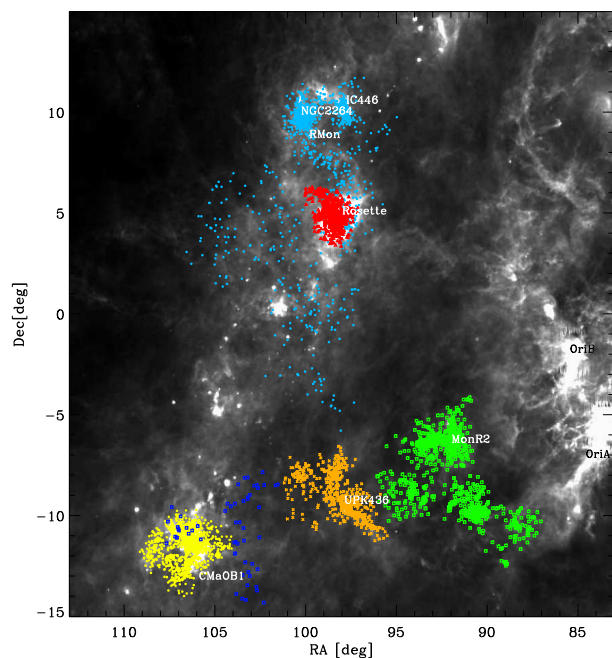


Fig. 8. Spatial distribution in Equatorial coordinates of the YSOs associated to NGC 2264, NGC 2244, Mon R2, CMA OB1 and UPK 436. YSOs are overplotted on a IRIS $100\mu\text{m}$ image (Miville-Deschênes & Lagache, 2005). For clarity, Orion members have not been plotted.

tion corresponding to the more distant Rosette Nebula, located at ~ 1.5 Kpc, hosting the SFR NGC 2244. Thus, our finding is that the known cluster NGC 2264 actually belongs to a structure larger than the $\sim 2^\circ \times \sim 2^\circ$ region, typically considered in the literature for this SFR. The mean distance of YSOs associated to the complex NGC2264-IC448 is 731.86 ± 95.5 pc, even though the proper motion distributions of the three subgroups suggest they share similar but not equal values.⁸

⁸ A detailed kinematic analysis of these sub-regions is beyond the aims of this work.

In the same region, we identified further 5 sub-structures with distance > 0.5 Kpc⁹, the most populated being the cluster in the CMA OB1 association, centered around RA=106.3° Dec=-11.47°, at a distance of 1250 ± 162 pc, associated to the Reflection Nebula IC 2177, including 1709 YSOs. In addition, we identified the cluster NGC 2244, including 810 YSOs, centered at RA=98.3° Dec=4.9°, at a distance of 1580 ± 199 pc and the cluster associated to Mon R2, at a distance of 897 ± 112 pc, including 1272 YSOs. In addition, we detected the cluster indicated in Cantat-Gaudin & Anders (2020) as UPK 436 with 620 members and a minor sparse cluster in the region of CMA OB1 located at 807 pc.

Figure 9 shows PM, parallaxes and CAMD of all these sub-structures, where it is clearly visible that they are spatially and kinematically uncorrelated, while in the PMS region of the CAMD they are indistinguishable since they consist of similar age stars.

The membership defined in Flaccomio et al. (2022) includes two levels of confidences. One based on the combination of several criteria derived by dedicated X-ray, spectroscopic and IR observations, including 2263 confirmed members (sample C) and where the fraction of false positives is negligible and another list (sample C-Wide), based exclusively on all-sky surveys, including 1542 YSOs, where the membership has been deduced by a smaller number of criteria and thus the number of false positives is expected to be higher. We find that the YSOs of the sample C (sample C-Wide) in common with our list of YSOs in the NGC 2264 region are 972 (960), corresponding to a fraction of 43% (62%) with respect to the Flaccomio sample. These fractions are considered here as indicators of our level of completeness of the entire SFR population. However, these results are strongly conditioned by the starting photometric selection ($M_G > 5$) and the restrictions on the *Gaia* EDR3 data that we adopted in this work. In addition, the Flaccomio et al. sample C includes 497 of the 2263 confirmed members that do not have a *Gaia* counterpart.

To estimate the efficiency of our method to recover YSOs, we considered the members selected by Flaccomio et al. with a *Gaia* counterpart, falling in the photometric region considered in this work, and compliant with our initial data restrictions (i.e. $RUWE < 1.4$ and parallax relative error < 0.2). Adopting this sample, the fraction of the YSOs selected by us in common with the Flaccomio et al. membership is 95%-96%, considering both

⁹ This limit has been adopted to avoid the Orion sub-structures

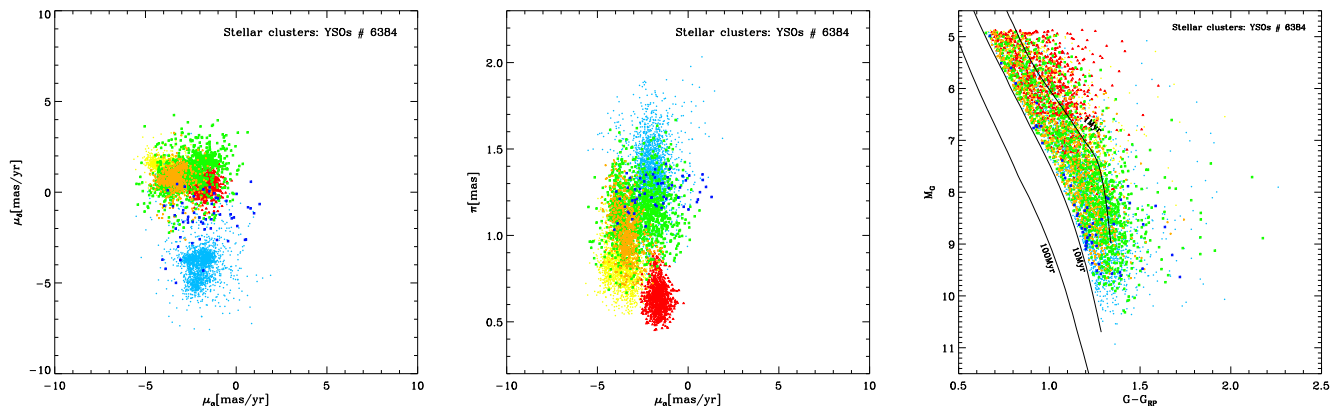


Fig. 9. Proper motions in RA and Dec, parallaxes and CAMDs of the SFRs falling in the field of view of NGC 2264. The symbol colors of the clusters are as in Fig. 8. Three representative solar metallicity isochrones computed from the Pisa models are also shown.

the samples C and C-Wide. We note that this is the efficiency of our clustering method but is not the efficiency of the *Gaia* data. In fact, if for the two lists, we consider the members falling in the same photometric region but we do not consider the restrictions in *RUWE* and in the parallax error, the fraction of YSOs in common is 72% for sample C and 77% for sample C-wide. This suggests that 23%-28% of genuine YSOs are missed by us due to remaining issues in the *Gaia* data, at least in the current *Gaia* EDR3 release.

Finally, we find that among the 1 052 YSOs selected by us in the NGC 2264 region, a total of 1 034 are included in the list of objects collected by Flaccomio et al. but 62 of them are not members in the more complete and less contaminated sample C. This means that about 92% i.e. (1 034-62)/1 052 of the YSOs selected by us are confirmed members. Hence we conclude that the contamination level of the sample that we have selected is $\sim 8\%$.

For comparison, in the same region, Kounkel & Covey (2019) found 637 YSOs, belonging to the clusters named as Theia 41 and 189, with 548 and 89 objects, respectively. Of them, 420, i.e. about 66%, are in common with our list.

6. Discussion

In the previous sections, we described how overdensities in the 5D parameter space (l , b , π , μ_{α^*} , μ_{δ}) have been identified, starting from a photometrically selected sample, that covers the expected PMS region of YSOs with ages $t < 10$ Myr.

Since no attempt has been made to correct for interstellar reddening, the starting sample was contaminated also from older reddened stars. Another possible reason for the contamination of older stars derives from the adopted strategy to select the starting sample in the plane M_G vs. $G - G_{BP}$, where the sensitivity to stellar ages of the available isochrones is quite low for the low mass population. In fact, for faint and very low-mass stars, isochrones get closer and closer for ages larger than about 50-100 Myr and, consequently, it is difficult to separate young populations from the older ones. As a result, the DBSCAN clustering algorithm, adopted to resolve spatially concentrated and/or co-moving stellar populations located at the same distance, can select also clusters older than 10 Myr.

A pattern match procedure has been adopted to disentangle SFRs and young clusters from older and photometrically unphysical clusters. We found 354 SFRs with ages $t \lesssim 10$ Myr and

322 young clusters with ages approximately in the range 10-100 Myr. We discuss here these validated findings in the context of the GP structure within ~ 1.5 kpc from the Sun.

The maps of the young stellar clusters recognised by the DBSCAN clustering algorithm, most of them already known in the literature, have been shown in the previous sections, and specific spatial and kinematic details have been presented for some of them.

To identify clusters extended on scales larger than the $5^\circ \times 5^\circ$ boxes used in the analysis, we merged adjacent clusters with consistent proper motions and distances. This procedure has been applied to identify extended SFRs as a whole, as in the case of the Orion Complex or Sco OB2 UCL, with r_{50} equal to $\simeq 17^\circ$ and $\simeq 15^\circ$, respectively, that are among the most extended structures resolved in this work. In several cases, it identifies clusters that encompass multiple populations, as in the case of NGC 2264, that has been identified as a unique structure including also the close cluster IC 446 and other YSOs in the surrounding region. A more in depth analysis of the two clusters shows that their proper motions can be distinguished into slightly different sub-populations and thus our overall procedure to define clusters tends to include multiple sub-populations sharing similar properties, likely associated to the progenitor molecular cloud.

The question of the cluster and subcluster identification is a very complex issue that can be dealt at different spatial precision levels, required for a given analysis, as done, for example, for the MYStiX project, in Feigelson (2018), where a parametric statistical regression approach, providing hierarchical ellipsoid structures, has been adopted. The evidence of a wide range of central surface densities found in the MYStiX maps is in agreement with the different spatial morphology of the SFRs identified in this work.

Figure 10 shows the spatial distribution of the young stellar clusters found in this work, in three different bins of distance, [100, 600] pc, [600, 2000] pc and [100, 2000] pc. The young clusters are drawn by distinguishing them in the age bins $t < 10$ Myr, $10 \text{ Myr} < t < 100$ Myr and $t < 100$ Myr. Note that clusters with $10 \text{ Myr} < t < 100$ Myr have been found only in the solar neighbourhood (< 600 pc) and thus are shown only in the [100, 600] pc distance range.

The distribution of SFRs ($t < 10$ Myr) within 600 pc is dominated by the presence of big young structures crossing the GP such as the Orion and Perseus Complexes, Gamma Velo-

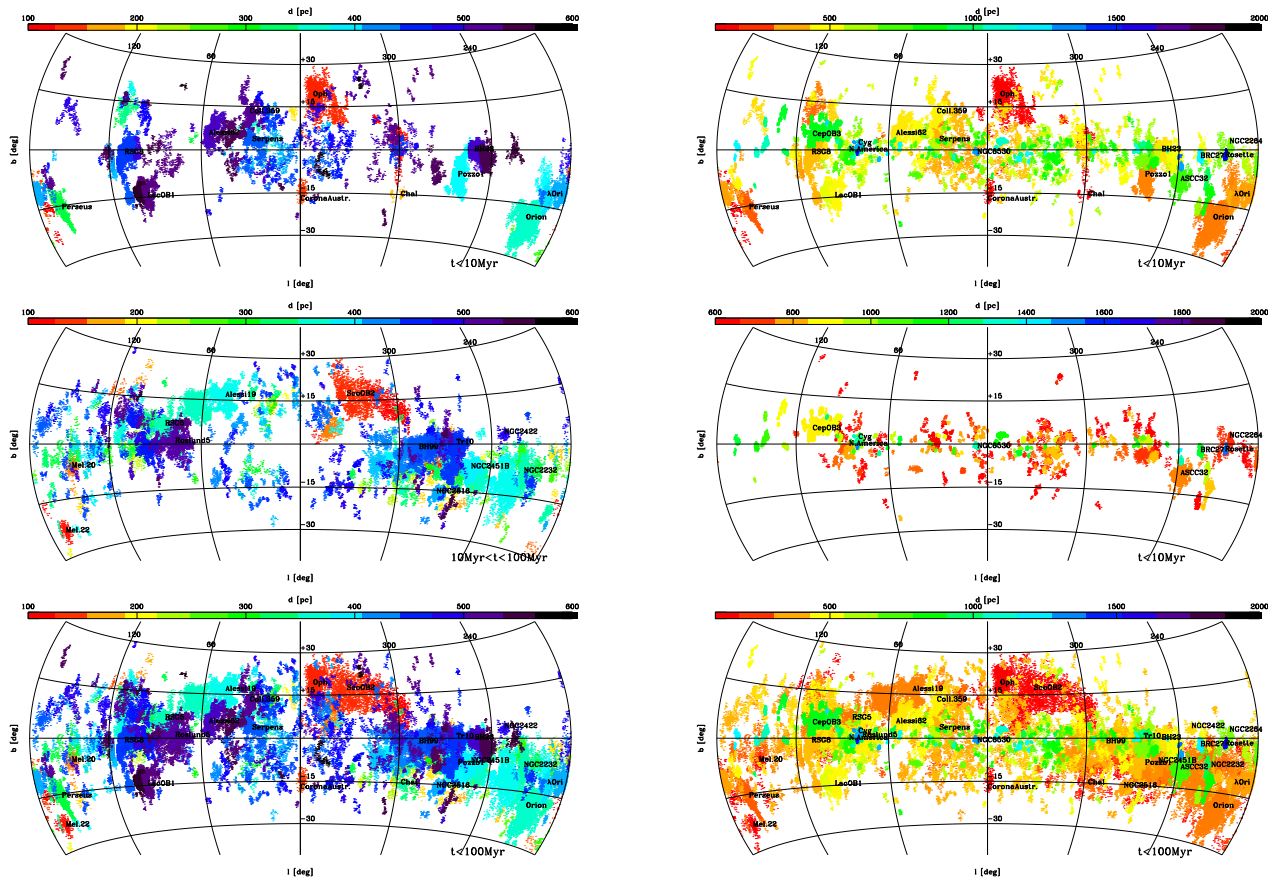


Fig. 10. Aitoff projections in Galactic coordinates of the YSOs in the different age bins ($t < 10$ Myr, $10 \text{ Myr} < t < 100$ Myr and $t < 100$ Myr), with distance in the range ($[100, 600]$ pc (left panels), $[600, 2000]$ pc (mid right panel) and $[100, 2000]$ pc (upper and bottom right panels). Color codes indicate stellar distances.

rum (Pozzo 1), Lac OB1, under the GP, BH 23 (corresponding to Theia 80 in Kounkel & Covey, 2019) and RSG 8 close to the GP, Serpens, Alessi 62, Collinder 359 and Rho Ophiuchi, over the GP. The clusters with ages $10 \text{ Myr} < t < 100 \text{ Myr}$ in the same distance range appear definitely more diffuse. Apart from the well known Sco-Cen association covering $\sim 60^\circ$ in longitudes, we detected as unique complex the likewise huge association in the Vela-Puppis region, including Trumpler 10, γ Velorum, NGC 2457, NGC 2451B, as well as the associations around NGC 2232, Roslund 5 and Alessi 19.

Their positions appear to be connected to the clusters with $t < 10$ Myr since they follow a spatial pattern crossing or very close to that of the SFRs. This suggests that they likely belong to a common star formation process encompassing at least two generations of YSOs, with the first generation including extended populations of dissolving young clusters and associations.

The large Sco-Cen association is connected to the Vela and Orion Complexes, confirming what already found by Bouy & Alves (2015) with Hipparcos data. These three regions are described there as three large-scale stream-like structures.

Going towards larger distances ($d \gtrsim 600$ pc), the SFRs show a more regular pattern, approximately parallel to the GP. The most prominent SFRs are ASCC 32 and Cep OB3b in the Cepheus, respectively under and over the GP at distance of ~ 800 - 900 pc. Among the most distant SFRs with more than 300 members and distance $\gtrsim 1400$ pc, we detected NGC 2244, NGC 6530, NGC 6531, NGC 2362 and FSR 0442.

The overall distribution of YSOs in SFRs with $d \lesssim 600$ pc traces a complex 3D pattern in the solar neighbourhood. In par-

ticular, in the Z vs. X edge-on Galactic projection (see bottom/left panel in Fig. 4 and top/left panel in Fig. 10) we find evidence of a projected inclined structure, mainly traced by the Orion, Vela OB2 and Rho Ophiuchi star forming complexes in the third and fourth Galactic quadrants and, by the Serpens, Lacerta OB1 and Perseus in the first and second Galactic quadrants. However, the SFRs falling in the Cepheus region do not follow this pattern. A global view of these structures and their spatial correlation with the surrounding nebular emission, suggests a pattern consistent with the results found in Molinari et al. (2010), where massive proto-clusters and entire clusters of YSOs in active SFRs are associated to clouds that collapse into filaments.

As already found in Zari et al. (2018), current data reveal a very complex 3D structure that cannot be simply described with the *Gould Belt*, i.e. the giant flat structure, inclined by $\sim 20^\circ$ with respect to the Galactic Plane, first pointed out by Gould (1879). This insight was already suggested by Guillout (2001), who presented the first detection of the *Gould Belt* late type star population, and who proposed the alternative scenario of a *Gould disk*.

A more detailed representation of the young Galactic component in the Solar Neighborhood has been recently proposed by Alves et al. (2020), who determined the 3D distribution of all local cloud complexes by deriving accurate distances to about 380 lines of sight. They suggested that such 3D distribution could be described by a damped sinusoidal wave, that they call Radcliffe Wave, with an amplitude of ~ 160 pc and a period of ~ 2 Kpc. It crosses Orion, around a minimum, Cepheus (crest), North Amer-

ica and Cygnus X. This structure is separated and distinct from a second structure, indicated as "split", crossing Sco-Cen, Aquila and Serpens clouds. They propose that the *Gould Belt* is a projection effect of two linear cloud complexes. The spatial distribution of YSOs associated to SFRs that has been identified in our work shows much more complex and diffuse structures but, the two elongated linear structures suggested by Alves et al. (2020) approximately cross the borderline of the two separated structures visible in the X, Y map of Fig. 4, delimited by the SFRs indicated by Alves et al. (2020). This brings us to confirm that the local young Galactic component is very complex. While our data are broadly consistent with the Alves et al. (2020) findings, further investigations, including a more detailed analysis of the kinematics of the structures, based on the 3D space coordinates (X, Y, Z) and velocities (U, V, W) (e.g. de Zeeuw et al., 1999) are required to confirm the scenario and to find additional insights about their origin.

To gain further insights on the star formation history of the SFRs, it is crucial to derive more accurate stellar ages. However, we do not attempt to derive stellar ages of the selected YSOs, for several reasons: first of all, the lack of a suitable photometric system. In fact, the large *Gaia* EDR3 G and RP photometric bands used for this work are not sensitive to the fundamental stellar parameters (effective temperatures, stellar ages, etc...), especially for low mass stars. However, future *Gaia* releases, overcoming issues related to the BP bands at faint magnitudes, could be crucial to this aim. Second, the lack of spectroscopic data needed to derive individual stellar reddening values, to appropriately place these YSOs on the HR diagram. Alternative ways, such as the use of 3D reddening maps (e.g. Bovy et al., 2016; Lallement et al., 2019), require careful analysis, since the integrated extinction tends to be underestimated in the molecular clouds, where SFRs are typically located. A detailed analysis is deferred to future works based on the combination of *Gaia* and spectroscopic data from available surveys, such as *Gaia*-ESO (Gilmore et al., 2012; Randich et al., 2013), LAMOST (Zhao et al., 2012) or APOGEE (Majewski et al., 2017), or future surveys such as WEAVE (Dalton et al., 2012) and 4MOST (Guiglion et al., 2019).

7. Summary and conclusions

We used the machine learning unsupervised clustering algorithm DBSCAN to systematically identify all SFRs with ages $t \lesssim 10$ Myr, within ~ 1.5 Kpc from the Sun. The density-based clustering algorithm has been applied to the *Gaia* EDR3 positions, parallaxes and proper motions of a photometrically-selected starting sample.

A pattern match procedure based on a template data set including typical clusters detected within the photometric sample has been used to distinguish very young clusters from the contaminant old clusters and from photometrically unphysical clusters. We provide here a catalogue with the main parameters (positions, spatial extent, median distance and number of members) of the 354 SFRs with ages $t \lesssim 10$ Myr. The parameters of the 322 young clusters with ages $10 \text{ Myr} \lesssim t \lesssim 100 \text{ Myr}$ are also given. We provide also the list of the 124 440 plus 65 863 YSOs found in the SFRs and the young clusters, respectively, including mainly late type K-M stars. A substantial number of YSOs have been recognized for the first time. Based on the comparison of our list of YSOs in the well known region Sco-Cen and NGC2264, we roughly estimate that, within our observational limits, the completeness of the census of cluster members obtained with our analysis is $\gtrsim 85\%$, at least in very rich and con-

centrated SFRs. For low density regions, such as the Taurus-Auriga association (see Appendix C), this completeness figure is expected to be around 50%. The mass function coverage of each cluster, strongly depends on the cluster distance, and is set by the observational limit.

Compact regular clusters, as well as SFRs in large complexes such as, for example, Taurus, Orion, Sco-OB2, Perseus, and Cygnus, have been identified with high efficiency, as estimated from the comparison with other available catalogues (see Appendix C).

The overall distribution of these clusters in the Galaxy context shows that they are distributed along a very complex 3D pattern that seems to connect them at least within 500-600 pc. Outside of this distance, the clusters appear to be more regularly and closely distributed along the GP.

As far as we know, the catalogue of YSOs presented in this work is the sole all-sky catalogue based on the most recent *Gaia* EDR3 data, which benefit of major improvements with respect to *Gaia* DR2. This catalogue represents a step forward in the census of SFRs and can be used, for example, for further detailed interpretations of their spatial distribution in the context of the spiral arm model (Reid et al., 2019), since it covers a substantial region crossed by the Local arm and, marginally, some regions of the Perseus and Sagittarius-Carina arms (Poggio et al., 2021). Future and photometric deep surveys, such as the Rubin Legacy Survey of Space and Time (LSST) will allow to extend these limits.

We note that these results are not at this stage suitable for studies such as star formation history, cluster dynamics, based on the full space 3D velocity determination, or IMF, since the census of the SFRs is not complete and accurate masses and ages, as well as radial velocities can not be determined, until further data are available. Nevertheless, the dominant component of the SFRs has been detected and thus these results can be used as driving samples for the extraction of complete populations from *Gaia* data, by relaxing the stringent constraints adopted in this work.

Finally, the SFRs identified in this work are defined well enough to allow detailed studies of circumstellar disk evolution and direct imaging of young giant planets, based on multiband analysis of available or future additional observations (X-rays or IR or radio), targeting some of the individual clusters.

Acknowledgements. This work has made use of data from the European Space Agency (ESA) mission *Gaia* (<https://www.cosmos.esa.int/gaia>), processed by the *Gaia* Data Processing and Analysis Consortium (DPAC, <https://www.cosmos.esa.int/web/gaia/dpac/consortium>). Funding for the DPAC has been provided by national institutions, in particular the institutions participating in the *Gaia* Multilateral Agreement. E.T. acknowledges Czech Science Foundation GACR (Project: 21-16583M). JMA acknowledges financial support from the project PRIN-INAF 2019 "Spectroscopically Tracing the Disk Dispersal Evolution. The authors are very grateful to the anonymous referee, for providing constructive comments and suggestions which significantly contributed to improving this publication.

References

- Alves, J., Zucker, C., Goodman, A. A., et al. 2020, *Nature*, 578, 237
- Anders, F., Khalatyan, A., Chiappini, C., et al. 2019, *A&A*, 628, A94
- Avedisova, V. S. 2002, *Astronomy Reports*, 46, 193
- Bailer-Jones, C. A. L., Rybizki, J., Fouesneau, M., Demleitner, M., & Andrae, R. 2021, *AJ*, 161, 147
- Bica, E., Pavani, D. B., Bonatto, C. J., & Lima, E. F. 2019, *AJ*, 157, 12
- Bonito, R., Prisinzano, L., Guarcello, M. G., & Micela, G. 2013, *A&A*, 556, A108
- Bouy, H. & Alves, J. 2015, *A&A*, 584, A26
- Bovy, J., Rix, H.-W., Green, G. M., Schlafly, E. F., & Finkbeiner, D. P. 2016, *ApJ*, 818, 130

- Bressan, A., Marigo, P., Girardi, L., et al. 2012, *MNRAS*, 427, 127
- Cantat-Gaudin, T. & Anders, F. 2020, *A&A*, 633, A99
- Cantat-Gaudin, T., Anders, F., Castro-Ginard, A., et al. 2020, *A&A*, 640, A1
- Cantat-Gaudin, T., Jordi, C., Vallenari, A., et al. 2018, *A&A*, 618, A93
- Castro-Ginard, A., Jordi, C., Luri, X., et al. 2020, *A&A*, 635, A45
- Castro-Ginard, A., Jordi, C., Luri, X., et al. 2018, *A&A*, 618, A59
- Chabrier, G. 2003, *PASP*, 115, 763
- Chen, W. P. & Lee, H. T. 2008, in *Handbook of Star Forming Regions*, Volume I, ed. B. Reipurth, Vol. 4, 124
- Chen, Y., Girardi, L., Bressan, A., et al. 2014, *MNRAS*, 444, 2525
- Cody, A. M., Stauffer, J., Baglin, A., et al. 2014, *AJ*, 147, 82
- Dalton, G., Trager, S. C., Abrams, D. C., et al. 2012, in *Society of Photo-Optical Instrumentation Engineers (SPIE) Conference Series*, Vol. 8446, Ground-based and Airborne Instrumentation for Astronomy IV, ed. I. S. McLean, S. K. Ramsay, & H. Takami, 84460P
- Damiani, F., Micela, G., Sciortino, S., et al. 2006, *A&A*, 460, 133
- Damiani, F., Prisinzano, L., Pillitteri, I., Micela, G., & Sciortino, S. 2019, *A&A*, 623, A112
- de Zeeuw, P. T., Hoogerwerf, R., de Bruijne, J. H. J., Brown, A. G. A., & Blaauw, A. 1999, *AJ*, 117, 354
- Dell'Omodarme, M., Valle, G., Degl'Innocenti, S., & Prada Moroni, P. G. 2012, *A&A*, 540, A26
- Dias, W. S., Alessi, B. S., Moitinho, A., & Lépine, J. R. D. 2002, *A&A*, 389, 871
- Dutra, C. M. & Bica, E. 2002, *A&A*, 383, 631
- Ercolano, B., Picogna, G., Monsch, K., Drake, J. J., & Preibisch, T. 2021, *MNRAS*, 508, 1675
- Ester, M., Kriegel, H.-P., Sander, J., & Xu, X. 1996, in *Second International Conference on Knowledge Discovery and Data Mining*, ed. J. Simoudis, E. Han & U. Fayyad (Menlo Park, CA: AAAI Press), 226
- Fasano, G. & Franceschini, A. 1987, *MNRAS*, 225, 155
- Feigelson, E. D. 2018, in *Astrophysics and Space Science Library*, Vol. 424, *The Birth of Star Clusters*, ed. S. Stahler, 119
- Fernández-López, M., Arce, H. G., Looney, L., et al. 2014, *ApJ*, 790, L19
- Flaccomio, E., Micela, G., & Sciortino, S. 2006, *A&A*, 455, 903
- Franciosini, E., Tognelli, E., Degl'Innocenti, S., et al. 2021, arXiv e-prints, arXiv:2111.11196
- Gaia Collaboration, Brown, A. G. A., Vallenari, A., et al. 2021, *A&A*, 649, A1
- Gaia Collaboration, Prusti, T., de Bruijne, J. H. J., et al. 2016, *A&A*, 595, A1
- Gilmore, G., Randich, S., Asplund, M., et al. 2012, *The Messenger*, 147, 25
- Gould, B. A. 1879, *Resultados del Observatorio Nacional Argentino*, 1, 1
- Guiglion, G., Battistini, C., Bell, C. P. M., et al. 2019, *The Messenger*, 175, 17
- Guillout, P. 2001, in *Astronomical Society of the Pacific Conference Series*, Vol. 243, *From Darkness to Light: Origin and Evolution of Young Stellar Clusters*, ed. T. Montmerle & P. André, 677
- Gullbring, E., Hartmann, L., Briceno, C., & Calvet, N. 1998, *ApJ*, 492, 323
- Jackson, R. J., Jeffries, R. D., Wright, N. J., et al. 2022, *MNRAS*, 509, 1664
- Jeffries, R. D., Jackson, R. J., Franciosini, E., et al. 2017, *MNRAS*, 464, 1456
- Kerr, R. M. P., Rizzuto, A. C., Kraus, A. L., & Offner, S. S. R. 2021, *ApJ*, 917, 23
- Kervella, P., Arenou, F., & Thévenin, F. 2022, *A&A*, 657, A7
- Kounkel, M. & Covey, K. 2019, *AJ*, 158, 122
- Kounkel, M., Covey, K., & Stassun, K. G. 2020, *AJ*, 160, 279
- Kraus, A. L., Ireland, M. J., Hillenbrand, L. A., & Martinache, F. 2012, *ApJ*, 745, 19
- Krolikowski, D. M., Kraus, A. L., & Rizzuto, A. C. 2021, *AJ*, 162, 110
- Kronberger, M., Teutsch, P., Alessi, B., et al. 2006, *A&A*, 447, 921
- Krone-Martins, A. & Moitinho, A. 2014, *A&A*, 561, A57
- Lada, C. J. 2006, *ApJ*, 640, L63
- Lallement, R., Babusiaux, C., Vergely, J. L., et al. 2019, *A&A*, 625, A135
- Le Duigou, J. M. & Knödseder, J. 2002, *A&A*, 392, 869
- Lindegren, L., Bastian, U., Biermann, M., et al. 2021a, *A&A*, 649, A4
- Lindegren, L., Klioner, S. A., Hernández, J., et al. 2021b, *A&A*, 649, A2
- Liu, L. & Pang, X. 2019, *ApJS*, 245, 32
- Luhman, K. L. 2022, *AJ*, 163, 24
- Luri, X., Brown, A. G. A., Sarro, L. M., et al. 2018, *A&A*, 616, A9
- Majewski, S. R., Schiavon, R. P., Frinchaboy, P. M., et al. 2017, *AJ*, 154, 94
- Mathieu, R. D. 1994, *ARA&A*, 32, 465
- Mayne, N. J. & Naylor, T. 2008, *MNRAS*, 386, 261
- McInnes, L., Healy, J., & Astels, S. 2017, *JOSS*, 2, 205
- Megeath, S. T., Gutermuth, R., Muzerolle, J., et al. 2012, *AJ*, 144, 192
- Mitra-Kraev, U., Harra, L. K., Güdel, M., et al. 2005, *A&A*, 431, 679
- Miville-Deschênes, M.-A. & Lagache, G. 2005, *ApJS*, 157, 302
- Miville-Deschênes, M.-A., Murray, N., & Lee, E. J. 2017, *ApJ*, 834, 57
- Moitinho, A., Alves, J., Huéramo, N., & Lada, C. J. 2001, *ApJ*, 563, L73
- Molinari, S., Swinyard, B., Bally, J., et al. 2010, *A&A*, 518, L100
- Montalto, M., Piotto, G., Marrese, P. M., et al. 2021, *A&A*, 653, A98
- Otrupceek, R. E., Hartley, M., & Wang, J. S. 2000, *PASA*, 17, 92
- Palla, F., Randich, S., Flaccomio, E., & Pallavicini, R. 2005, *ApJ*, 626, L49
- Palla, F. & Stahler, S. W. 1999, *ApJ*, 525, 772
- Peacock, J. A. 1983, *MNRAS*, 202, 615
- Pecaut, M. J. & Mamajek, E. E. 2013, *ApJS*, 208, 9
- Piecka, M. & Paunzen, E. 2021, arXiv e-prints, arXiv:2107.07230
- Poggio, E., Drimmel, R., Cantat-Gaudin, T., et al. 2021, *A&A*, 651, A104
- Prisinzano, L., Damiani, F., Micela, G., & Sciortino, S. 2005, *A&A*, 430, 941
- Randich, S., Gilmore, G., & Gaia-ESO Consortium. 2013, *The Messenger*, 154, 47
- Randich, S., Tognelli, E., Jackson, R., et al. 2018, *A&A*, 612, A99
- Rebull, L. M., Johnson, C. H., Gibbs, J. C., et al. 2013, *AJ*, 145, 15
- Reid, M. J., Menten, K. M., Brunthaler, A., et al. 2019, *ApJ*, 885, 131
- Riello, M., De Angeli, F., Evans, D. W., et al. 2021, *A&A*, 649, A3
- Salpeter, E. E. 1955, *ApJ*, 121, 161
- Scalo, J. 1998, in *ASP Conf. Ser. 142: The Stellar Initial Mass Function (38th Herstmonceux Conference)*, 201
- Sitnik, T. G. 2003, *Astronomy Letters*, 29, 311
- Soderblom, D. R., Hillenbrand, L. A., Jeffries, R. D., Mamajek, E. E., & Naylor, T. 2014, *Protostars and Planets VI*, 219
- Somers, G., Cao, L., & Pinsonneault, M. H. 2020, *ApJ*, 891, 29
- Spina, L., Randich, S., Magrini, L., et al. 2017, *A&A*, 601, A70
- Tang, J., Bressan, A., Rosenfield, P., et al. 2014, *MNRAS*, 445, 4287
- Tognelli, E., Prada Moroni, P. G., & Degl'Innocenti, S. 2018, *MNRAS*, 476, 27
- Tognelli, E., Prada Moroni, P. G., Degl'Innocenti, S., Salaris, M., & Cassisi, S. 2020, *A&A*, 638, A81
- Venuti, L., Damiani, F., & Prisinzano, L. 2019, *A&A*, 621, A14
- Yonekura, Y., Dobashi, K., Mizuno, A., Ogawa, H., & Fukui, Y. 1997, *ApJS*, 110, 21
- Zari, E., Hashemi, H., Brown, A. G. A., Jardine, K., & de Zeeuw, P. T. 2018, *A&A*, 620, A172
- Zhao, G., Zhao, Y.-H., Chu, Y.-Q., Jing, Y.-P., & Deng, L.-C. 2012, *Research in Astronomy and Astrophysics*, 12, 723
- Zucker, C., Speagle, J. S., Schlafly, E. F., et al. 2020, *A&A*, 633, A51

Appendix A: Interstellar reddening effects

In this section we show the effects of the reddening on the sample selected as described in Section 3. As discussed in Anders et al. (2019), for a generic passband i , extinction coefficients A_i/A_V depend on the stellar effective temperature. The subsequent dust attenuated photometry of very broad photometric passbands, such as the *Gaia* EDR3 ones, is not a simple linear function of A_V , but it is also a function of the source spectrum i.e. its effective temperature.

The PARSEC 1.2S stellar models (Bressan et al., 2012; Chen et al., 2014; Tang et al., 2014) have been implemented to predict tracks and isochrones also at non-zero extinction. As done in Montalto et al. (2021), in order to have an indication of the reddening which affects our data, we used the CMD 3.3 input form web interface, and we constructed a grid of stellar models assuming the 1 Gyr isochrone, and $A_V=[0.1, 0.5, 1.0, 1.5, 2.0, 2.5, 3.0, 3.5, 4.0, 4.5, 5.0, 6.0, 7.0, 8.0, 9.0, 10.0, 20.0, 30.0]$.

Figure A.1 shows how the 1 Gyr isochrone changes by increasing extinction A_V from 0 to 10, in the CAMD obtained by adopting the different *Gaia* colors (panels a and b). The 1 Gyr isochrone at $A_V = 0$ is highlighted by a thick black line while the 1 Gyr isochrone at $A_V = 3$ is highlighted by symbols with different shades of pink in the different stellar evolution phases.

Note that the reddened isochrone is not linearly shifted along a reddening direction, as usually happens when adopting a reddening vector. For example, for an object at $M_G = 3$, corresponding to a star with $(G_{BP}-G_{RP})_0=0.47$, $(G-G_{RP})_0=0.30$ and effective temperature of 6930 K at 1 Gyr (black empty square in the Figure) with extinction $A_V = 3$, the reddening $E(G_{BP}-G_{RP})$ is equal to 1.24 and $E(G-G_{RP})$ is equal to 0.55 (blue arrows in the Figure). But, for an object at $M_G = 8$, corresponding to a star with $(G_{BP}-G_{RP})_0=1.81$, $(G-G_{RP})_0=0.90$ and effective temperature of 3945 K at 1 Gyr (black bullet in the Figure) with extinction $A_V = 3$, the reddening $E(G_{BP}-G_{RP})$ is equal to 1.09 and $E(G-G_{RP})$ is equal to 0.26 (red arrows in the Figure).

Thus, at different temperatures, and for a fixed A_V , the shift in color due to the reddening is smaller for the colder star. And this effect is higher in the G vs. G- G_{RP} diagram, as can be deduced from the different slopes of the blue and red arrows. In this case, for a ~ 4000 K star, the $E(G-G_{RP})$ value (equal to ≈ 0.26) is about half than the one (≈ 0.55) associated to a ~ 7000 K star.

This implies that while a reddened 1 Gyr old star with effective temperature of ~ 7000 K can be expected to be found in the PMS region and mimic a star younger than 10 Myr, a colder star of ~ 4000 K, of the same age and affected by the same extinction, does not fall in the PMS region (see Fig. A.1, panel b). In conclusion, the effect of uncorrected reddening in terms of contamination of our initial photometric sample by old stars is larger for stars with spectral type F and G, than for K and M stars.

Appendix B: The effect of binarity or multiplicity on astrometric selections

At the level of astrometric sensitivity offered by *Gaia*, the orbital motions of binary (or multiple) stars become sometimes measurable, and also difficult to disentangle from proper motion. This holds both for resolved pairs, and for unresolved unequal-mass pairs where the photocenter displays significant motion (see Kervella et al., 2022). If the binary period resonates with the *Gaia* sampling frequency, parallax measurements will be also affected. Perhaps the best-studied star-forming region in terms of its binary-star population is Taurus-Auriga, and we may refer to the review by Mathieu (1994) to get an idea of the expected

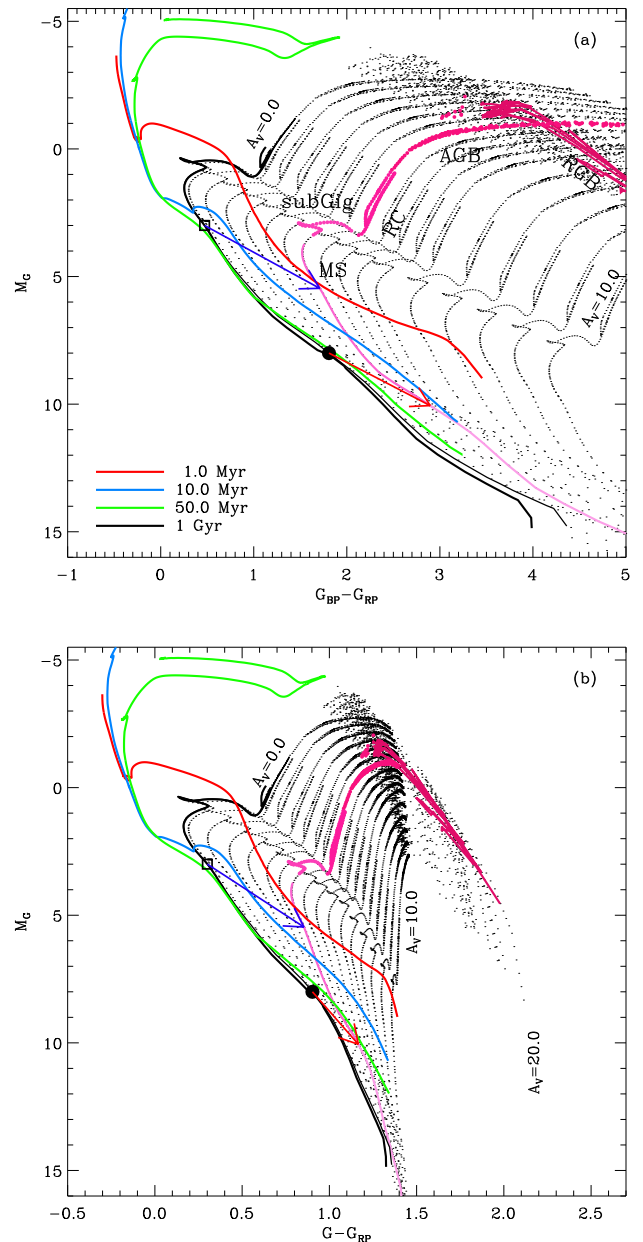


Fig. A.1. PARSEC 1 Gyr isochrone at solar metallicity with extinction A_V ranging from 0 to 10.0 in the CAMD obtained by adopting the different *Gaia* magnitudes (black dots). The 1 Gyr isochrone at $A_V = 0$ is highlighted by a thick black solid line. The 1 Gyr isochrone at $A_V = 3$ is highlighted by pink coloured lines of different shades during the Red Giant Branch (RGB), Asymptotic Giant Branch (AGB), Red Clump (RC), sub Giants (subGig) and MS phases. The red, light-blue and green solid lines are the 1, 10 and 50 Myr Pisa isochrones at solar metallicity. The empty square and the bullet in each panel represent a star of 6930 K and 3945 K, respectively, while the blue and red arrows are the reddening vectors corresponding to $A_V = 3$, for these two representative stars (see text).

range of system parameters. Taurus is one of the few SFRs where lunar occultation techniques were feasible for detection of close pairs, down to separations of $0.009''$ (Mathieu, 1994, Table A1 and references therein). Therefore, the projected binary separations range across a factor of ~ 1000 , with no “typical” value. Correspondingly, their orbital periods span a range of a factor of ~ 30000 .

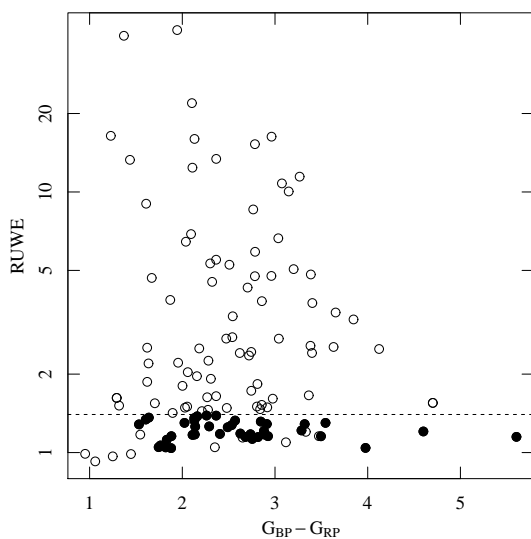


Fig. B.1. Diagram of the RUWE values vs. the Gaia color $G_{BP}-G_{RP}$ of the Kraus et al. (2012) Tau-Aur binary-star list with *Gaia* EDR3 counterparts. Filled symbols are the binaries selected also in this work, while empty symbols are those rejected.

We have checked empirically if the Gaia-based selection used in this paper keeps the binary members of a SFR, by matching the Tau-Aur binary-star list in Table 1 from Kraus et al. (2012) with the *Gaia* EDR3 catalogue, and with its subset selected in this paper. Out of 156 stars in Kraus et al., we found 142 *Gaia*-EDR3 counterparts within $0.5''$, of which 40 selected in this work using DBSCAN.

We have then compared the RUWE distributions of the selected vs. the unselected systems, to gain insight on how binary motions impact RUWE and the subsequent selection. Figure B.1 shows a diagram of RUWE vs. *Gaia* color $G_{BP}-G_{RP}$. The horizontal line indicates our maximum accepted RUWE value. Filled symbols are stars passing our selection, while empty symbols are the unmatched binaries, i.e. those not retrieved in our catalogue. It should be remembered that the cut in absolute- G magnitude rejects some stars which would have passed the RUWE constraint. Nevertheless, the vast majority of unmatched stars have indeed RUWE values well above the chosen limiting value, and were likely rejected for this reason. There is little or no dependence of RUWE on *Gaia* color, and therefore mass (although part of color spread is also due to high extinction towards Tau-Aur). Also interesting is the diagram shown in Fig. B.2, showing RUWE vs. binary separation. Here, the absence of any dependence of RUWE on projected separation (when measurable) is very evident, including unresolved pairs, where only the photocenter is affected by orbital motion. This latter diagram contains only 6 out of 40 stars selected by us, since about one-half of the Kraus et al. pairs are spectroscopic binaries with no measured separation. We also point out that out of the 76 binaries with no measured separation, 32 pass our selection (42%), while only 8 out of the 66 binaries with measured separation pass the selection (12%), probably because photocenter motion has a smaller effect on astrometry compared to the motion of resolved components. Overall, extending this result from Tau-Aur to other SFRs

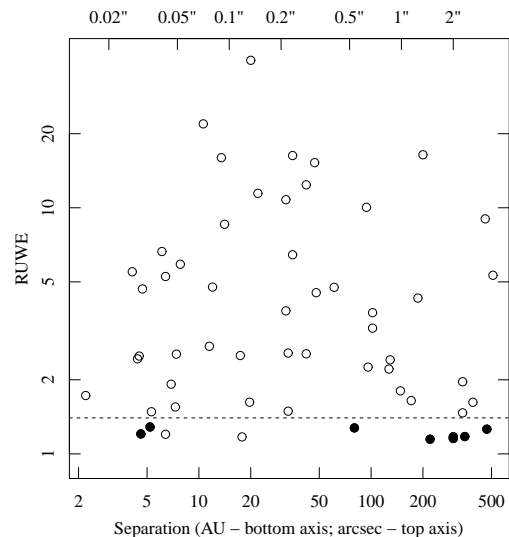


Fig. B.2. Diagram of the RUWE values vs. the binary separation of the Kraus et al. (2012) Tau-Aur binary-star list with *Gaia* EDR3 counterparts. Symbols are as in Fig. B.1.

at similar distances, we would predict to have lost $\sim 72\%$ of their binary populations due to our selection criteria. Thus, if a binary frequency is as high as 50% (Mathieu, 1994), a loss of $\sim 35\%$ of PMS members can be expected. However, since this work selects stars at distances up to ~ 1500 pc, this estimate should not be naively extended to our whole sample: the larger the distance the smaller the projected binary motions hence, closer to our detection limit. We therefore expect a less significant binary member loss for the farther-out SFRs. A more detailed study of these effects would however be far beyond the scope of this paper, also taking into account that the upcoming *Gaia* data release DR3 (foreseen June 2022) will contain orbital astrometric solutions for 135 760 non-single stars¹⁰.

Appendix C: Literature comparison

Appendix C.1: The Taurus-Auriga association

The Taurus-Auriga complex is one of the nearest active SFRs of low mass stars to which many works have been dedicated. In this region, we identified several substructures, as can be seen from Fig. C.1. In order to identify the YSOs associated to the Taurus-Auriga association, we imposed the upper distance limit equal to 225 pc, as done in Krolkowski et al. (2021), and restricted the spatial region in the range $58.0^\circ < RA < 86.0^\circ$ and $10.5^\circ < Dec < 38.5^\circ$. We considered the sub-structures whose members are all within these limits. With these conditions we identified a total of 313 YSOs associated to 6 substructures. The spatial distributions are shown in Fig. C.1, while PMs, parallaxes and the CAMD are shown in Fig. C.2.

The members in the southwest subregion (light blue plus symbols in the Figures) are distributed quite close to the 10 Myr isochrone and then they could be part of an older population unselected by us for the photometric cut we used. But, with the exception of this, the members of the other substructures show

¹⁰ See <https://www.cosmos.esa.int/web/gaia/>

the typical distribution of stars in PMS. The PMs of the substructures are quite well distinct, as well as parallaxes, suggesting a complex 3D structure with the known core including members in the region $63.0^\circ \leq RA \leq 70.0^\circ$ and $23^\circ \leq Dec \leq 28^\circ$ (blue star symbols in the Figures), being also on the close side (median distance equal to 132 pc). The easternmost and most populated substructure (red square symbols in the Figures) is, instead, the most distant (median distance equal to 171 pc). A marginal evidence of age spread, as found in Krolkowski et al. (2021), is also found with our analysis but our results cannot be considered conclusive being based on reddening uncorrected photometry.

Krolkowski et al. (2021) compiled, very recently, the most complete and inclusive census of members of this region found in the literature. Among these, 587 objects have *Gaia* EDR3 counterparts, with 528 having a full astrometric solution. Using the *Gaia* EDR3 identification number given in the Krolkowski et al. (2021) table, we matched the list of the 437 Taurus members in the Krolkowski et al. (2021) table that are included in the photometric limits imposed in our work, with the YSOs with $t < 10$ Myr (i.e. classified with flag from 1 to 28), and found 202 objects in common, that amount to about 46% (202/437) of the Krolkowski et al. (2021) list and 65% (202/313) of our list of YSOs in this region. We note that the Krolkowski et al. (2021) list has been obtained from the compilation of previous works, including local spectroscopic and IR data surveys that do not homogeneously cover the entire region as we have done with *Gaia* data. For example, many of the 111 YSOs not included in the Krolkowski et al. (2021) table belong to the clusters 579 and 572 in Table 3 that includes 88 and 30 YSOs (red squares and light blue symbols in Fig. C.1, top panel), in two sub-regions poorly covered by Krolkowski et al. (2021).

We compared the list of YSOs in Taurus also with the list of members identified as excess of mass (EOM) by Kerr et al. (2021) using *Gaia* DR2 data. Details on the match with our catalogue are given in Sect. C.4. As in our case, Kerr et al. (2021) found substructures beyond the distance of known members. To perform a consistent comparison, we restricted the Kerr et al. (2021) catalogue in RA, Dec and distance, as done for our catalogue. Those identified as EOM in this region are 429. Among these, we considered the ones with $G > 7.5$ and $M_G > 5$, to match the same photometric region adopted for our catalogue. Of the 409 Kerr et al. (2021) YSOs that meets these conditions, we found that 197 (about 48%) are in common with our list of YSOs. We note that a rigorous consistent comparison is very hard to perform, since it strongly depends not only on the adopted clustering techniques but also on the subsample of *Gaia* data that is selected as starting point of the subsequent analysis.

The Taurus region is a well known complex structure in which the membership has been very hard to achieve due to its large spatial extent and strong obscuration by the nebula. The comparison we have done is sufficient to assert that about 50% of the selected YSOs in this region are already found in other surveys and that they are distributed in sub-structures that are consistent with those found in other works, in particular with the results presented by Kerr et al. (2021), that homogeneously cover the entire region.

Appendix C.2: The Orion Complex

YSOs associated to the Orion complex have been identified by selecting objects with $75^\circ < RA < 90^\circ$ and $-11^\circ < Dec < 10^\circ$. In this way, we found 18 840 YSOs associated to 7 substructures

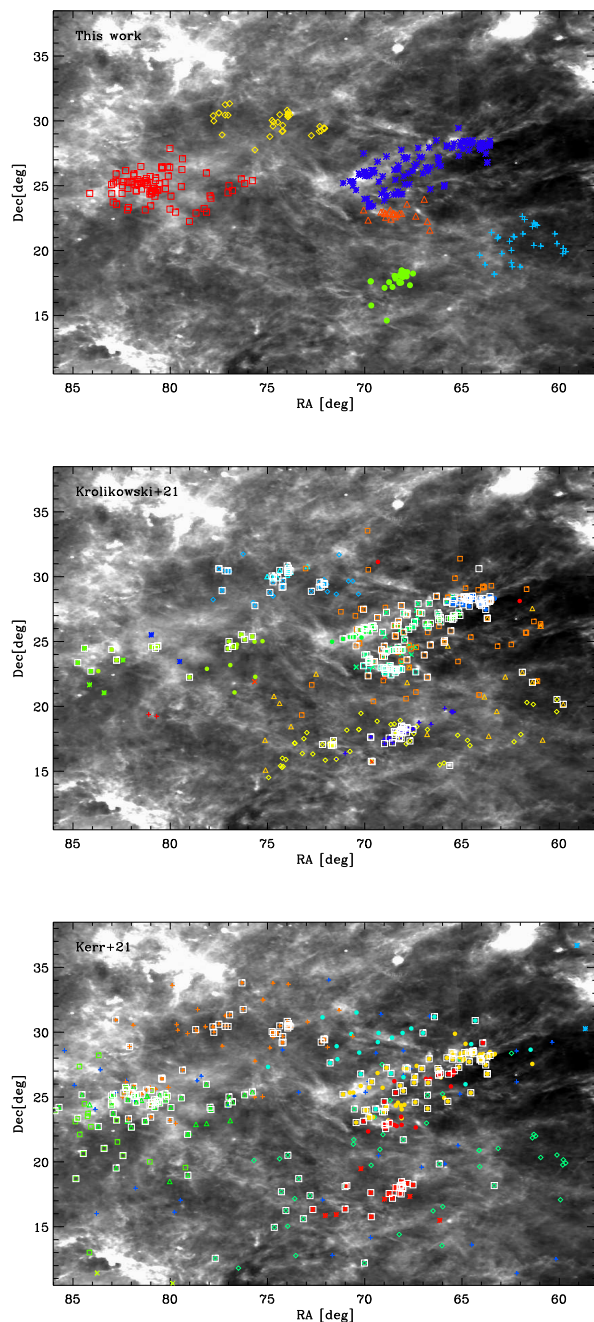


Fig. C.1. YSOs associated to the Taurus-Auriga Association, selected in this work (upper panel), in Krolkowski et al. (2021) (middle panel) and Kerr et al. (2021) (lower panel). Colors and symbols indicate the substructures found by us with DBSCAN, those derived by the Gaussian mixture model (GMM) in Krolkowski et al. (2021) and those derived as EOM by Kerr et al. (2021). White boxes in the middle and lower panels indicate the YSOs in common with our catalogue. YSOs are overlotted on a IRIS $100 \mu\text{m}$ image (Miville-Deschênes & Lagache, 2005).

with $t \lesssim 10$ Myr. These are shown in Fig. C.3¹¹, where we note the presence of already known substructures such as λ and σ Ori, ONC, 25 Ori. All the main sub-structures covering the Orion A and B Nebulae have been merged by our procedure in a single complex including 14 832 YSOs and further 1 576 YSOs in the

¹¹ For a direct visual comparison, spatial limits of the figure are the same used in Fig. 1 of Kounkel & Covey (2019).

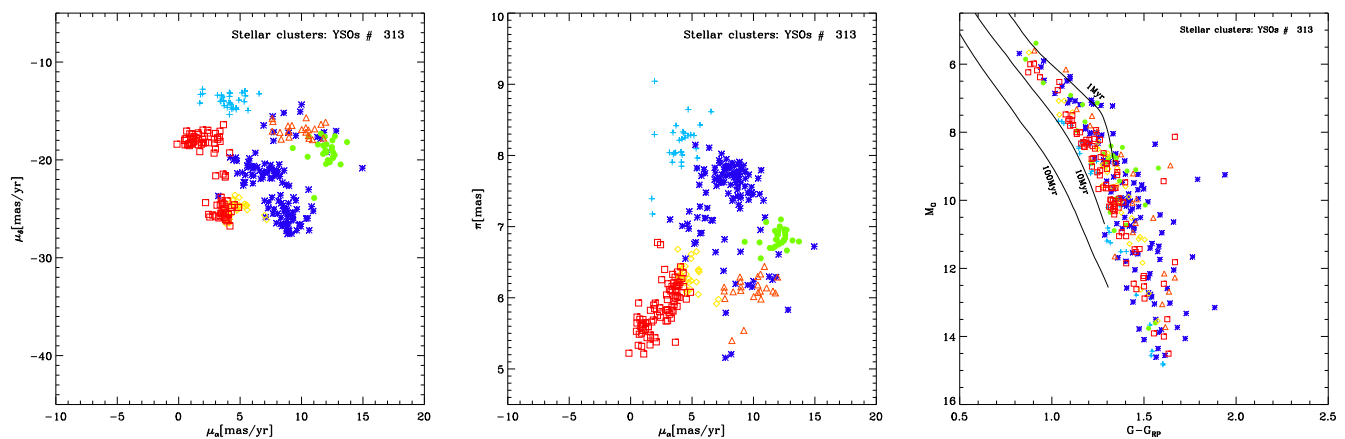


Fig. C.2. Proper motions in RA and Dec, parallaxes and CAMDs of the clusters associated to the Taurus-Auriga complex. Three representative solar metallicity isochrones from the Pisa models are also shown. Symbols and colors are as in Fig. C.1.

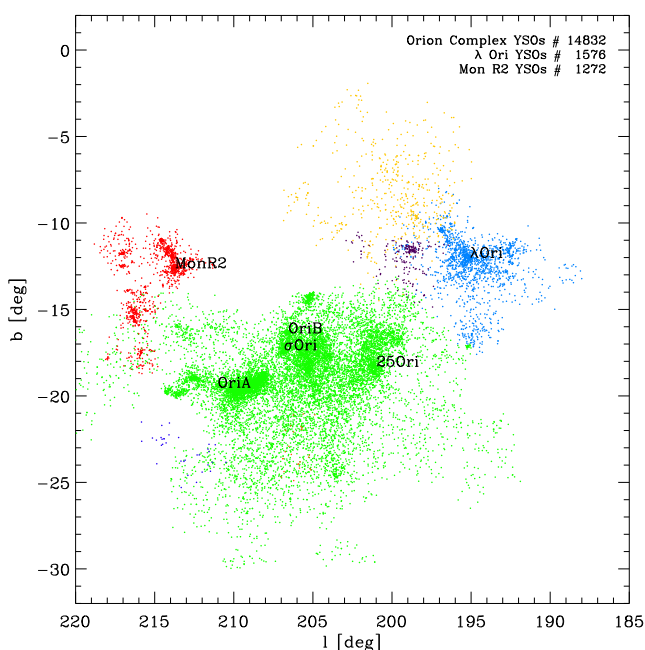


Fig. C.3. Spatial distribution in Galactic coordinates of the YSOs associated to the Orion Complex. YSOs identified in the 7 substructures are drawn with different symbols and colors.

λ Ori cluster. The most distant cluster associated to Monoceros R2 (Mon-R2) is not part of the close Orion Complex and includes 1 272 YSOs with a mean distance of 897 pc ($\sigma = 123$ pc).

Figure C.4 shows proper motions and parallaxes of the substructures found in the Orion area. In particular, the proper motions show a very complex kinematic pattern of the subclusters in this region. However, a detailed analysis of the Orion kinematics is beyond the aims of this work.

Figure C.4 also shows the CAMD of the populations associated to Orion. Even though we can not rigorously interpret it, being our data not corrected for reddening, we note an apparent large age spread for all the populations.

We compare our findings in the Orion Complex region with the Kounkel & Covey (2019) catalogue. Details on the match between the two catalogues are given in Sect. C.4. To retrieve the YSOs identified by Kounkel & Covey (2019) in the Orion Com-

plex, we considered from their Table 2, the 16 structures (Theia groups) falling in the Orion region as defined above. The YSOs in the Kounkel & Covey (2019) and Kounkel et al. (2020) catalogues associated to the Theia groups of the Orion Complex are 11 882 and 10 373, respectively. Those in common with the list of Orion members found in this work are 7 983 (67%) and 7 822 (75%).

The Orion Complex has been extensively investigated with Spitzer IR data. For example, the Megeath et al. (2012) catalogue includes 3 479 YSOs stars¹² that cover a quite extended region of the Orion A and B nebulae. Using the cross-match service provided by CDS, Strasbourg, and a matching radius of $1''$, we found that 2 612 IR sources from the Megeath et al. (2012) catalogue have a *Gaia* EDR3 counterpart. From this sample, we considered only those with photometric and astrometric restrictions given in equation 1, with $G-G_{RP} > 0.58$ and in the range $203^\circ < l < 216^\circ$ and $-30^\circ < b < 30^\circ$, that amount to 1 667 YSOs. Of these, 1 561 ($\sim 94\%$) are identified by us members of the Orion Complex. The spatial distributions of our members and those found in Megeath et al. (2012) are shown in Fig. C.5. This high percentage proves that *Gaia* data have an efficiency in accurately diagnosing membership of YSOs in SFRs comparable to that of IR data. If we consider the subsample of 2 612 Megeath et al. (2012) objects with *Gaia* counterparts, and assume that it includes only genuine YSOs (i.e. 0% of contamination), we can conclude that our completeness level is about 60%. This value is the result of the restrictions we imposed to our initial data set to reduce the contamination level. We note that we can have a significant bias against (missed) binary stars. In fact, if we only discard the condition $RUWE < 1.4$, and retain the other conditions, the Megeath et al. (2012) YSOs *Gaia* counterparts are 1 953 and this implies that 286 YSOs (1953-1667), i.e. about 14% of the total sample (very likely binary systems), are missed in our data set. We do not attempt to estimate the fraction of false positives that could be included in our sample by considering the Megeath et al. (2012) catalogue since it includes mainly Class II stars, i.e. YSOs with IR excess emission from the circumstellar disk and it is therefore incomplete for the Class III stars, that do not show excess emission in the IR.

¹² retrieved at http://astro1.physics.utoledo.edu/~megeath/Orion/The_Spitzer_Orion_Survey.html

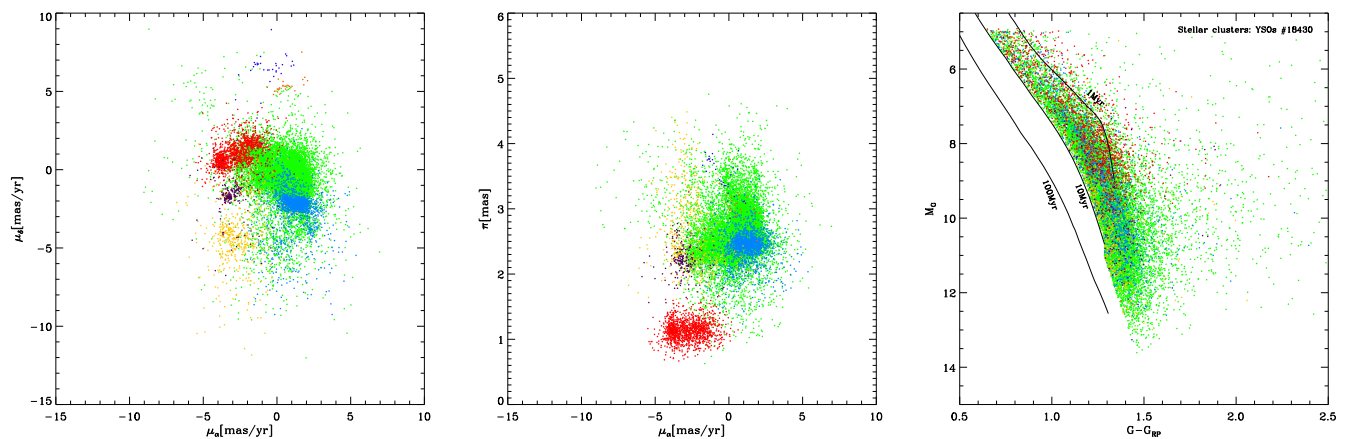


Fig. C.4. Proper motions in RA and Dec, parallaxes and CAMDs of the YSOs associated to the Orion complex. The symbol colors of the sub-clusters are as in Fig. C.3. Three representative solar metallicity isochrones from the Pisa models are also shown.

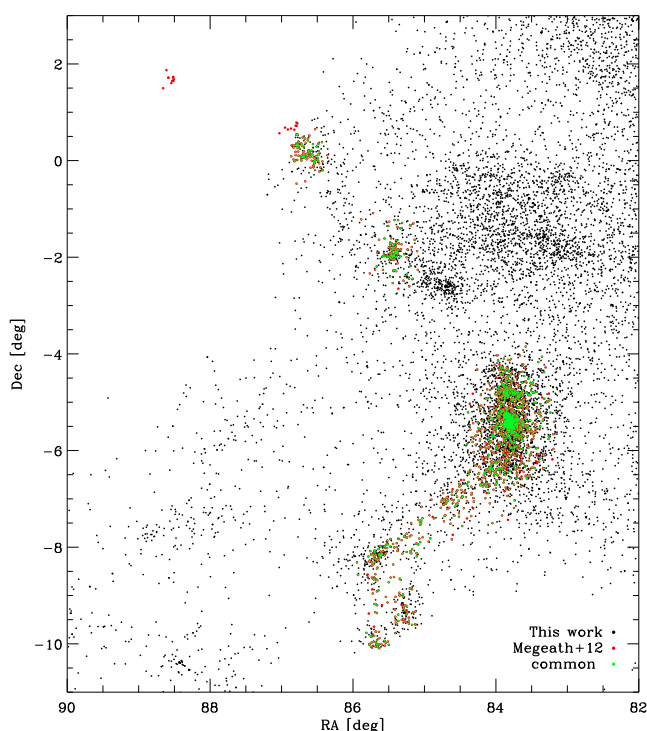


Fig. C.5. Spatial distribution of the Orion YSOs compared to YSOs found in Megeath et al. (2012), indicated as black and red symbols, respectively. YSOs in common to the two catalogues are drawn as green symbols.

Appendix C.3: The interstellar dust free SFR NGC 2362

At a distance of 1354 ± 192 pc, NGC 2362 is a SFR characterised by a very low and uniform reddening, estimated to be $E(B-V)=0.1$ (Moitinho et al., 2001). For this reason, the cluster shows a small spread in the optical V vs. V-I diagram, as found by Moitinho et al. (2001) and confirmed by Damiani et al. (2006) and this enables to constraint the duration of the star formation process that in this region has been about 1-2 Myr (Damiani et al., 2006). This result has been derived on the basis of a Chandra-ACIS X-ray observation, pointed in the cluster, from which a list of very likely members has been obtained. As for the case of NGC 2264, this cluster has been found with

our procedure in a region more extended than that investigated by Damiani et al. (2006). The 879 YSOs compatible with being members of NGC 2362 are plotted in Fig. C.6. Within the nominal cluster center $l=238.2^\circ$, -5.54° (Damiani et al., 2006), we found 150 candidate members while the others are mostly concentrated around the three bumps visible in the IR image. A further subgroup of cluster members shows an aligned spatial distribution roughly going from NGC 2362 to the H II region LBN 1059.

To compare our data, with the list of 387 X-ray members by Damiani et al. (2006), we cross-matched this list with the *Gaia* EDR3 catalogue, by using the cross-match service provided by CDS, Strasbourg, adopting a matching radius of $0.5''$. We find that 294 of them have a single *Gaia* EDR3 counterpart but those that are compliant with our initial data set restrictions and falling in the PMS region of the CAMD compatible with ages < 10 Myr are 129. Among these, 118, i.e. $\sim 91\%$, are in common with our list of YSOs. This fraction confirms that, even though our list of YSOs is incomplete, due to the significant fraction of members discarded a priori with the adopted data restrictions, in the adopted photometric ranges, the efficiency of our method in detecting very likely members is very high, if we consider that X-ray detections select YSOs without any bias based on the stellar evolutionary status (Class II or III YSOs), with an high efficiency in the spectral types (G to M) we are working on.

Within the Chandra-ACIS field of view, we selected a total of 150 YSOs, and 32 of them (21%) are not X-ray detected. X-ray detections found in Damiani et al. (2006) are complete for masses larger than $0.4 M_\odot$, that, assuming the cluster age of 4-5 Myr (Mayne & Naylor, 2008), corresponds to $M_G \simeq 7.5$. By considering that more than 50% of these X-ray undetected YSOs are fainter than this limit and that most of them are located far from the cluster center, where the Chandra-ACIS spatial resolution is lower, we are confident that the 32 X-ray undetected YSOs classified by us are likely members.

As for the other clusters, we investigated proper motions, parallaxes and CAMD, that are shown in Fig. C.7. The proper motion scatter plot indicates that actually the distribution of YSOs falling in the Chandra-ACIS is more concentrated than that of the overall cluster, which shows an inclined trend. This confirms that the entire cluster is characterised by a kinematic structure slightly more complex than that of the subgroup of YSOs falling around the known cluster center. The parallax val-

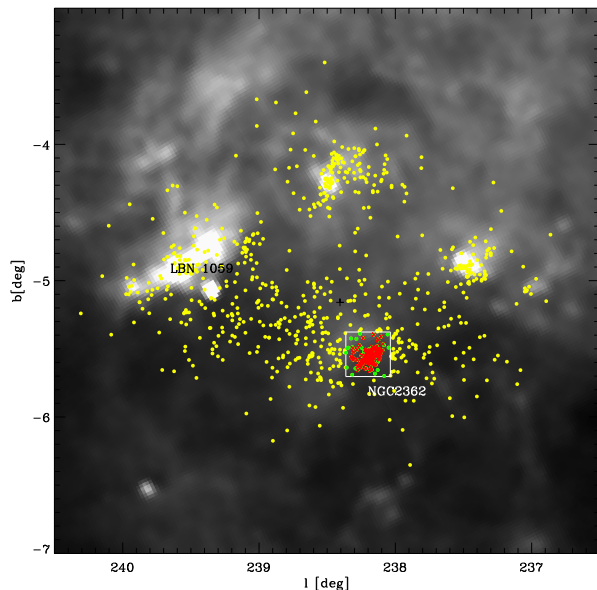


Fig. C.6. Spatial distribution in Galactic coordinates of the YSOs associated with NGC2362 (yellow symbols). YSOs falling in the box of $16.9'' \times 16.9''$ equal to the Chandra-ACIS field (white box) used in Damiani et al. (2006) are indicated as green symbols. YSOs in common with Damiani et al. (2006) X-ray detections are indicated as red symbols. Objects are overplotted on a IRIS $100 \mu\text{m}$ image.

ues indicate that all the detected YSOs are located at consistent distances.

We note that to reduce the observed spread in the M_G vs. $G - G_{RP}$ diagram shown in Fig. C.7, in the computation of M_G , we used the median cluster distance, rather than the individual member distances. The residual observed luminosity spread in the M_G vs. $G - G_{RP}$ diagram is likely due to reddening effects not corrected here and that, on the contrary, are very small in the V vs. V-I diagram, where the reddening vector is almost parallel to the cluster sequence in the low mass range (see Fig. 4 in Damiani et al. (2006)).

Appendix C.4: Comparison with literature all-sky star cluster catalogues

Using the *gaiaedr3.dr2_neighbourhood* table in the Gaia archive, we retrieved the *Gaia* DR2 identification number of the candidate YSOs selected in our work and thus, using these IDs, we performed the match with the Kerr et al. (2021) list, including 30 518 YSOs within 333 pc and selected with *Gaia* DR2. We found a total of 9 351 objects in common. Among these, 4 676 are associated to clusters with $t \lesssim 10$ Myr and 3 914 are associated to clusters with $10 \text{ Myr} \lesssim t \lesssim 100$ Myr of our catalogue.

Using the same procedure for the Kounkel & Covey (2019) and Kounkel et al. (2020) catalogues, that include 288 370 entries up to 1 Kpc and 987 376 entries, up to 3 Kpc, respectively, we find a total of 38 567 and 42 350 YSOs in common. Those associated to SFRs with $t \lesssim 10$ Myr (young clusters with $10 \text{ Myr} \lesssim t \lesssim 100$ Myr) are 23 071 (9 494) for the Kounkel & Covey (2019) list, and 25 511 (9 559) for the Kounkel et al. (2020) list. The remaining common stars have been discarded by us since they do not belong to the young age range. We note that, while in the contest of the entire all-sky cat-

alogue the fraction of objects in common is very low ($\sim 13\%$ and $\sim 4\%$), in the region of the Orion Complex it is 67% and 75% (see Sect. C.2). However, we note that our catalogue does not include the string-like massive clusters at ≥ 1 kpc, with spatial distribution aligned to the GP, that we discarded in the cluster validation phase (see Sect. 4.2). Instead, the Kounkel & Covey (2019) and Kounkel et al. (2020) lists include many of these objects and this could explain the low fraction of objects in common with respect to the entire catalogue. In addition, the restrictions to the initial data set are very different. For example, we imposed a photometric selection in the extinction uncorrected M_G vs. $G - G_{RP}$ CAMD, aimed to select mainly objects with age < 10 Myr. On the contrary, in the Kounkel & Covey (2019) and Kounkel et al. (2020) catalogues, no photometric selection has been applied and in fact these catalogues includes up to ~ 1 Gyr old clusters.

We compared our results also with the list of 2017 clusters recently published by Cantat-Gaudin & Anders (2020) that includes 234 128 cluster members. They used the most complete list of clusters from the literature and assigned them cluster membership using the UPMASK procedure (Krone-Martins & Moitinho, 2014), that is based on the compactness of the groups in the positional space and it is constrained to a fixed field of view. For 1 867 of these clusters, reliable parameters have been derived.

We find that the members presented by Cantat-Gaudin & Anders (2020) in common with our catalogue are 12 438. Those associated to SFRs ($t \lesssim 10$ Myr), young ($10 \text{ Myr} \lesssim t \lesssim 100$ Myr) and old ($t \geq 100$ Myr) clusters are 6 788, 2 519 and 2 109, respectively, corresponding to 66, 38 and 76 clusters in our catalog, in the same age ranges. They belong to 311 clusters of the Cantat-Gaudin & Anders (2020) list¹³ with parallaxes > 0.617 mas, that, approximatively, corresponds to the maximum distance of YSOs identified in our work. In the Cantat-Gaudin & Anders (2020) catalogue, the cluster members with $\pi > 0.617$, $G > 7.5$ and $M_G > 5.0$ are in total 49 074 and therefore we find that only $\sim 25\%$ of YSOs detected by us are in common with Cantat-Gaudin & Anders (2020). Using the ages derived in Cantat-Gaudin & Anders (2020), we find that 226 of the matched clusters are older than 10 Myr.

For the 331 clusters in common, we compared the distances assigned by Cantat-Gaudin & Anders (2020) computed as the inverted parallaxes of the value given for each cluster and the mean distance obtained by us, computed from the weighted mean parallaxes. Errors on the parallaxes were computed as the error on the mean. The comparison is shown in Fig. C.8, where the mean and standard deviation of the residuals between the two measurement sets are also given. The two determinations are consistent, even though there is a bias due to the different *Gaia* data realises adopted in our work (EDR3) and in Cantat-Gaudin & Anders (2020) (DR2).

¹³ This apparent discrepancy is due to the fact that our catalogue includes merged clusters that can include more than one cluster in the Cantat-Gaudin & Anders (2020) list.

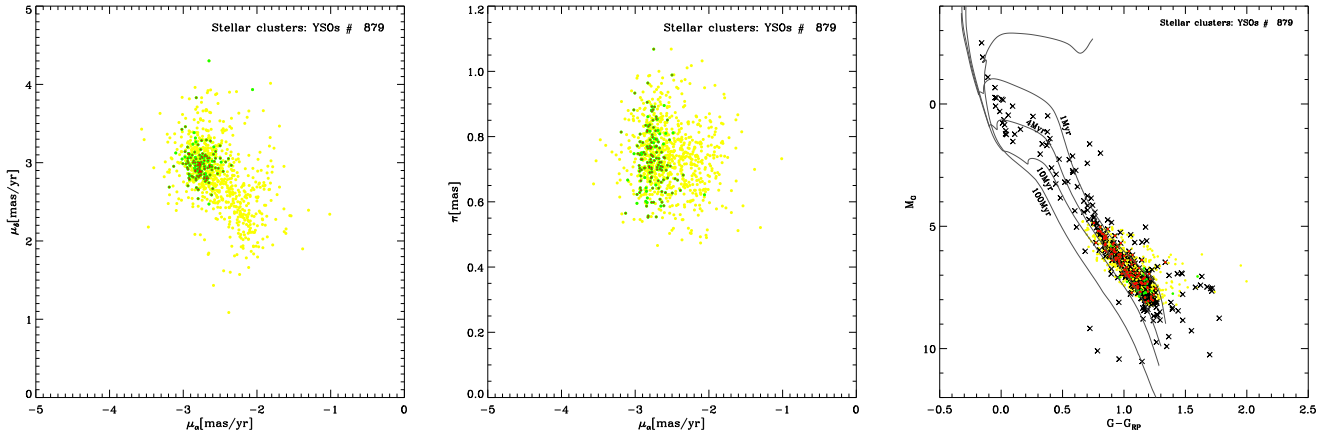


Fig. C.7. Proper motions in RA and Dec, parallaxes and CAMDs of the YSOs associated to NGC 2362. Symbol colors are as in Fig. C.6. Black x symbols are the X-ray detected YSOs by Damiani et al. (2006). Four representative solar metallicity isochrones from the Pisa models are also shown.

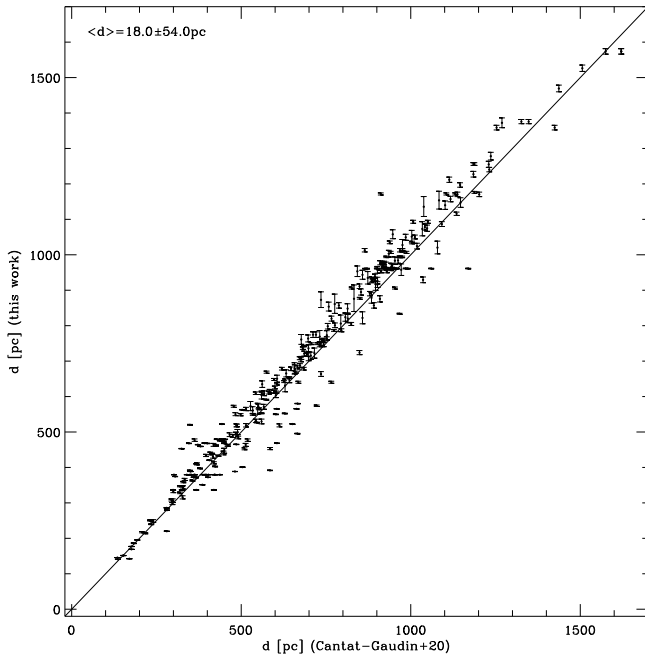


Fig. C.8. Comparison between the cluster distances derived by Cantat-Gaudin & Anders (2020) and those derived in this work. The line with slope one is shown for guidance.

Table 3. SFRs with $t \lesssim 10$ Myr (flag from 1 to 28) and young stellar clusters with $10 \text{ Myr} \lesssim t \lesssim 100$ Myr (flag from 29 to 36) found in this work. r_{50} is the radius in which half of the identified members are concentrated, d is the distance obtained by inverting the median value of the member parallaxes and N is the number of members.

ID	l [deg]	b [deg]	r_{50} [deg]	d [pc]	N	Flag	Name
1	-96.449	0.072	12.478	472	2275	36	Trumpler 10
2	-94.538	-8.490	11.040	465	2290	30	NGC 2547
3	-94.465	-7.524	6.055	181	119	32	
4	-93.624	-3.647	5.498	727	1041	16	IC 2395
5	-92.666	-13.246	4.699	260	59	32	
6	-91.409	-6.554	7.230	360	534	32	UPK 535
7	-90.205	3.832	6.919	530	265	36	
8	-89.938	-0.530	1.120	1157	60	7	
9	-89.504	-6.745	3.085	152	145	34	IC 2391
10	-89.466	-9.069	2.698	220	30	32	
11	-88.284	0.172	6.961	455	875	36	
12	-88.154	-8.441	2.973	167	27	35	
13	-88.147	9.678	2.348	866	32	26	
14	-88.115	3.047	4.069	574	68	36	
15	-87.277	0.377	6.827	501	78	29	
16	-87.062	25.179	2.405	545	42	27	
17	-86.304	-3.375	3.821	529	44	29	
18	-86.236	-15.931	6.881	427	1156	33	NGC 2516
19	-85.195	8.550	3.617	609	79	27	
20	-84.673	-9.961	4.737	340	233	34	UPK 545
21	-83.696	-7.225	9.220	563	544	28	
22	-83.159	-2.574	5.196	777	162	26	NGC 2925
23	-82.931	-7.518	6.444	138	248	32	Platais 8
24	-82.855	-6.763	2.730	356	28	32	
25	-82.786	-24.990	3.226	439	50	36	
26	-81.504	-11.623	4.851	212	79	32	
27	-81.366	-0.482	8.796	463	1787	29	ASCC 58
28	-81.087	6.878	2.543	276	25	34	
29	-80.582	6.319	2.641	517	36	25	NGC 3228
30	-80.532	11.611	3.786	498	40	29	UPK 560
31	-79.282	4.535	2.913	487	153	30	NGC 3228
32	-78.954	-7.548	3.379	305	76	32	
33	-77.076	-17.426	3.108	208	28	34	
34	-76.627	1.131	2.966	882	83	16	
35	-76.416	25.251	3.224	554	38	25	
36	-75.250	-11.637	4.967	509	65	36	UBC 260
37	-74.108	12.813	5.029	486	83	33	
38	-73.928	17.492	2.609	540	57	36	
39	-72.798	-4.711	3.904	554	33	28	
40	-72.489	-12.872	4.050	551	93	36	UBC 260
41	-72.284	-1.572	10.742	455	3655	29	Alessi 5
42	-72.188	0.357	2.288	788	22	16	
43	-71.889	-5.182	4.232	473	44	33	
44	-71.817	-17.545	3.926	330	57	34	
45	-70.641	-20.407	2.544	669	31	27	
46	-70.480	-10.225	5.599	240	101	32	
47	-70.324	1.396	1.656	497	172	28	NGC 3532
48	-70.259	-5.011	6.825	151	315	32	IC 2602
49	-70.253	-7.547	3.824	429	26	31	UPK 567
50	-70.223	-4.455	1.806	363	22	32	
51	-70.086	-8.365	3.236	380	64	29	
52	-69.705	18.749	2.954	548	38	28	
53	-69.426	4.225	5.208	626	101	27	
54	-69.330	0.875	2.800	876	78	16	
55	-69.132	-4.132	5.011	537	63	28	
56	-69.052	-5.162	2.534	413	24	33	
57	-68.100	-4.103	4.205	540	67	36	
58	-67.315	7.267	4.693	517	62	19	

Table 3. continued.

ID	l [deg]	b [deg]	r_{50} [deg]	d [pc]	N	Flag	Name
59	-66.879	7.655	1.501	686	25	27	
60	-65.690	-10.675	4.568	404	96	33	
61	-65.300	-16.115	6.755	351	198	34	
62	-64.711	6.969	3.287	502	41	36	
63	-64.330	-0.385	1.390	1185	73	6	
64	-63.560	-10.898	1.323	526	26	36	
65	-63.533	-0.220	3.481	842	30	16	
66	-63.499	0.071	4.721	513	52	19	
67	-63.462	-1.949	3.186	835	56	16	
68	-63.411	-1.461	4.275	367	41	32	
69	-63.356	-10.062	8.543	271	436	32	
70	-63.190	-15.741	1.802	384	33	33	
71	-62.781	-15.444	3.099	192	156	20	Chamaeleon I
72	-62.690	4.155	2.735	107	51	24	
73	-61.658	4.076	2.648	831	67	26	ESO 130 06
74	-61.187	-4.006	10.159	444	1233	29	Ruprecht 98
75	-60.798	-1.916	3.818	532	59	36	
76	-59.826	-2.170	7.787	106	191	25	
77	-59.394	9.199	3.735	348	33	34	
78	-58.761	11.202	12.124	121	651	31	
79	-58.150	-0.831	5.034	543	52	17	ASCC 73
80	-58.143	0.107	8.144	467	386	28	Ruprecht 98
81	-58.111	-18.173	4.288	255	51	35	
82	-57.732	-18.447	2.945	210	23	32	
83	-57.451	19.431	2.651	438	33	36	
84	-57.143	4.739	5.854	112	235	24	[DB2002b] G302.72+4.67
85	-56.783	26.717	3.562	478	30	36	
86	-56.363	-14.720	2.452	200	41	14	Chamaeleon II
87	-56.362	2.081	4.365	362	44	31	
88	-55.370	6.046	9.153	542	414	28	
89	-54.299	-6.635	2.652	538	54	36	
90	-53.796	-22.279	3.472	571	67	28	
91	-53.725	-1.190	4.056	732	52	16	
92	-53.207	-6.366	11.272	404	868	29	
93	-52.196	-15.704	1.759	511	21	29	
94	-51.910	1.209	8.012	444	285	29	
95	-51.238	-9.538	4.132	491	54	36	
96	-50.877	2.052	2.568	628	28	27	
97	-49.679	-7.806	5.337	501	36	36	
98	-48.320	2.686	2.568	861	122	16	Loden 1194
99	-48.060	3.228	3.535	675	71	16	Loden 1194
100	-47.919	-7.163	1.139	768	25	16	
101	-47.703	16.496	4.409	451	88	29	
102	-47.066	-9.068	5.856	543	63	28	
103	-46.946	16.930	11.511	135	548	31	
104	-46.658	-16.710	1.952	470	22	29	
105	-46.201	23.216	2.013	681	110	26	UPK 599
106	-45.913	-9.476	2.137	617	54	25	
107	-45.882	2.815	4.942	524	40	28	
108	-45.822	10.062	2.771	130	61	24	
109	-45.818	-6.268	9.931	415	1061	29	BH 164
110	-45.048	-6.321	2.378	839	42	16	
111	-44.964	10.146	3.092	487	30	28	
112	-44.918	1.998	5.095	440	147	29	
113	-44.476	-4.009	4.454	540	48	28	
114	-43.532	21.171	0.996	722	44	15	
115	-43.372	-10.966	2.372	700	50	27	
116	-42.613	-16.142	2.640	686	25	27	
117	-42.540	0.077	3.590	602	57	27	
118	-42.276	-0.584	4.667	801	238	16	NGC 5662

Table 3. continued.

ID	l [deg]	b [deg]	r_{50} [deg]	d [pc]	N	Flag	Name
119	-42.086	-13.354	3.820	291	40	34	
120	-41.840	23.609	6.561	536	132	27	
121	-41.180	-8.323	3.138	830	95	26	UPK 605
122	-40.358	1.463	2.511	973	131	12	UPK 604
123	-39.974	-3.076	5.595	881	1465	15	ASCC 79
124	-39.294	14.853	9.160	146	474	31	UPK 606
125	-38.526	-16.705	2.224	513	28	36	
126	-38.358	4.744	4.906	485	56	36	
127	-37.930	23.635	2.440	598	54	27	
128	-37.558	-15.414	2.930	239	59	33	UPK 612
129	-36.522	-5.103	3.528	768	88	16	NGC 6025
130	-36.385	-5.136	1.915	752	37	26	
131	-35.937	-7.678	5.601	612	49	27	NGC 6025
132	-35.845	-23.940	3.508	486	43	36	
133	-35.550	-3.162	4.211	859	286	16	NGC 6025
134	-35.353	25.323	2.668	506	42	27	
135	-35.242	-2.783	5.006	783	116	16	ASCC 79
136	-35.146	2.794	4.421	816	98	16	Alessi 8
137	-34.955	5.710	5.353	614	166	27	
138	-34.495	-0.820	0.958	1157	31	6	
139	-34.357	-6.955	3.935	489	127	36	UBC 11
140	-34.319	-8.929	1.721	880	42	16	
141	-34.065	6.880	1.249	779	27	26	
142	-32.055	1.201	3.242	658	48	26	
143	-31.519	19.108	3.371	533	57	27	
144	-30.956	-10.687	4.393	338	124	29	UPK 624
145	-30.355	-14.405	4.647	502	245	36	Alessi 24
146	-30.332	-1.346	1.920	726	24	16	
147	-29.642	-16.225	3.946	614	78	27	Alessi 24
148	-29.000	16.813	15.052	145	1189	31	Sco OB2 UCL
149	-28.818	-7.801	1.283	811	34	16	
150	-28.035	3.283	8.676	485	193	28	UBC 5
151	-27.731	-11.900	1.841	538	25	27	
152	-27.515	-7.862	5.209	648	113	27	
153	-27.169	1.306	3.830	880	97	15	
154	-27.134	-3.711	2.380	775	36	16	
155	-26.304	-20.305	3.455	507	60	36	
156	-26.193	1.683	2.104	714	63	16	
157	-25.812	-1.280	0.940	1111	42	9	
158	-25.154	-10.416	1.286	691	21	16	
159	-24.822	26.797	2.351	461	30	36	
160	-24.156	2.958	2.179	731	42	15	
161	-23.409	-1.561	2.521	1229	665	2	Ara
162	-23.323	-13.813	4.854	475	116	36	
163	-22.934	-3.816	5.746	498	98	36	
164	-22.917	5.684	5.359	396	92	29	
165	-22.436	-6.992	4.974	481	173	19	
166	-22.177	12.095	3.669	473	72	36	
167	-21.922	1.272	6.287	499	79	28	
168	-21.394	1.315	1.627	968	346	6	NGC 6178
169	-21.262	-3.375	4.151	716	53	16	
170	-21.202	-13.476	4.566	525	35	29	
171	-20.902	12.995	10.427	146	712	24	Lupus
172	-19.293	-2.011	3.171	1055	515	6	NGC 6250
173	-19.081	-3.044	1.881	1217	260	7	
174	-19.055	-14.679	3.622	478	69	36	
175	-18.864	26.943	2.669	431	24	36	
176	-18.493	2.933	3.725	499	68	28	
177	-18.258	-5.923	4.920	460	57	28	
178	-17.957	20.104	3.856	511	69	27	

Table 3. continued.

ID	l [deg]	b [deg]	r_{50} [deg]	d [pc]	N	Flag	Name
179	-17.888	-15.724	2.822	489	72	33	Mamajek 4
180	-17.647	4.588	3.457	494	71	19	
181	-17.473	14.274	3.775	434	77	29	
182	-16.732	4.839	9.090	177	846	31	Lupus
183	-16.066	8.394	3.455	421	56	28	
184	-15.746	-17.104	3.182	450	56	36	Mamajek 4
185	-14.410	-4.152	1.756	761	22	16	
186	-14.321	0.121	7.397	454	165	28	NGC 6281
187	-14.076	-7.758	4.203	597	82	27	
188	-13.473	10.580	7.085	448	317	36	
189	-13.420	20.566	1.833	505	31	30	
190	-13.175	-3.090	3.299	751	56	16	
191	-12.700	-9.280	2.708	474	35	36	
192	-11.829	6.743	3.367	458	44	36	
193	-10.960	-2.354	3.959	591	56	27	
194	-10.732	14.031	4.960	505	166	28	
195	-10.004	9.162	3.813	146	41	25	
196	-9.930	25.445	2.422	444	38	36	
197	-9.915	10.226	7.620	467	120	36	
198	-9.508	-8.086	3.002	470	31	25	UPK 645
199	-9.442	2.729	4.174	137	33	31	
200	-9.287	6.563	3.497	478	35	28	
201	-9.176	-16.263	1.956	564	27	27	
202	-9.066	-5.233	1.280	874	21	15	
203	-8.884	3.253	1.715	959	95	12	ASCC 88
204	-8.429	1.541	3.260	501	61	25	
205	-8.312	-6.509	4.201	143	32	24	
206	-8.044	-4.905	7.576	450	121	19	Collinder 338
207	-8.024	18.781	12.655	144	2398	22	Ophiuchus
208	-7.866	3.002	4.764	1169	2357	11	[DB2002b] G352.16+3.07
209	-7.710	-20.911	2.305	473	32	30	
210	-7.391	15.036	1.973	518	49	28	
211	-7.076	-17.920	2.195	476	34	28	
212	-4.794	5.832	1.955	471	27	25	
213	-4.533	0.198	1.692	1180	656	10	NGC 6383
214	-4.445	10.953	3.834	504	32	28	
215	-4.192	2.623	3.191	533	29	18	
216	-4.109	-6.571	4.014	488	38	27	
217	-2.395	-9.439	1.454	867	33	15	
218	-0.858	-13.905	3.965	150	208	24	
219	-0.255	6.752	3.380	148	43	24	
220	-0.132	-17.592	3.291	155	107	23	Corona Australis
221	0.403	4.777	0.914	808	27	12	
222	0.487	4.285	2.189	490	32	25	
223	0.567	6.000	3.526	472	56	18	
224	0.822	10.197	3.335	428	42	33	
225	0.837	-3.620	5.322	625	67	16	
226	1.003	-12.626	3.133	648	25	27	
227	2.347	-22.823	1.458	544	25	27	
228	2.803	2.699	1.903	856	58	15	
229	3.110	3.461	3.050	841	95	15	
230	3.520	22.428	6.797	430	153	29	
231	3.634	-6.585	3.077	732	155	16	
232	3.813	2.889	2.194	489	22	18	
233	3.874	15.233	3.476	429	109	33	
234	4.075	21.668	2.136	466	32	36	
235	4.194	-11.448	2.401	647	87	27	
236	4.544	13.042	3.333	212	74	22	
237	4.792	27.043	1.474	492	22	36	
238	5.632	-10.087	4.945	461	98	28	

Table 3. continued.

ID	l [deg]	b [deg]	r_{50} [deg]	d [pc]	N	Flag	Name
239	6.060	-1.287	1.020	1364	635	4	NGC 6530
240	6.075	5.472	1.609	801	37	15	
241	6.284	-5.757	1.562	866	41	15	
242	6.526	-0.629	7.200	451	124	17	
243	6.671	2.425	1.982	891	77	15	
244	7.137	17.593	4.456	223	39	35	
245	7.165	24.420	3.317	506	35	36	
246	7.367	5.609	3.870	715	110	13	NGC 6494
247	7.585	-0.338	1.634	1351	804	5	NGC 6531
248	7.892	-3.967	1.421	723	23	15	
249	9.679	6.527	2.603	785	40	16	
250	10.156	-10.852	4.019	460	85	36	
251	10.541	-16.488	5.479	494	123	36	
252	11.131	9.082	2.054	701	46	26	
253	11.186	-2.692	8.521	424	313	19	
254	11.469	10.028	3.752	490	63	28	
255	11.605	11.169	3.165	388	32	29	
256	11.697	2.667	0.704	745	24	16	
257	11.912	-12.956	2.069	577	41	27	
258	12.821	11.370	2.667	411	38	31	
259	13.334	23.368	2.803	468	45	36	
260	13.806	-9.612	3.760	369	30	32	ASCC 99
261	14.243	-14.327	4.405	441	61	29	UPK 12
262	14.457	-11.037	4.225	429	31	30	
263	15.190	-9.366	1.829	744	171	16	Collinder 394
264	15.293	-9.938	5.056	481	93	28	Ruprecht 145
265	15.519	11.502	4.538	473	70	28	
266	15.688	18.258	3.323	362	46	29	
267	15.716	3.599	5.558	410	56	28	
268	15.878	4.308	3.854	429	37	28	
269	16.123	13.603	5.040	313	68	34	
270	16.407	2.751	2.612	849	71	12	
271	16.537	5.969	4.495	425	44	28	
272	16.828	16.940	4.101	333	39	32	
273	17.190	-5.564	6.253	480	92	18	ASCC 97
274	17.215	12.634	4.622	205	92	35	Aquila Rift
275	17.298	-5.378	3.142	464	28	28	UPK 20
276	17.387	-3.582	2.091	908	42	12	
277	17.783	-3.847	0.976	853	32	12	
278	18.123	9.194	5.094	460	208	28	
279	18.177	-26.428	2.861	418	28	30	
280	18.197	-5.350	4.510	353	46	22	
281	18.517	16.294	4.909	231	46	35	
282	18.531	14.715	3.443	299	28	32	
283	19.348	-2.278	1.094	856	41	15	
284	19.519	13.840	4.769	434	64	28	
285	19.788	12.807	3.686	448	98	28	
286	19.802	6.630	2.169	305	27	32	
287	19.883	17.295	2.112	471	43	30	
288	19.922	-3.149	1.689	850	46	12	
289	19.946	-13.073	2.759	456	49	28	
290	20.015	13.080	1.283	474	31	28	
291	20.503	-2.228	1.297	1153	66	7	
292	20.989	12.856	3.462	480	64	28	
293	21.162	2.238	5.529	371	68	28	
294	21.213	4.420	4.778	354	36	31	
295	21.251	-19.125	2.072	472	33	36	
296	21.361	6.667	5.202	418	112	29	
297	22.142	-7.933	6.176	518	113	25	UPK 20
298	22.512	-0.950	4.183	430	35	17	UPK 24

Table 3. continued.

ID	l [deg]	b [deg]	r_{50} [deg]	d [pc]	N	Flag	Name
299	22.549	-1.320	0.981	759	35	16	
300	22.587	-12.951	1.788	437	25	30	
301	22.871	10.530	1.128	478	30	28	
302	22.964	11.793	2.919	506	38	28	
303	23.070	3.429	3.226	671	130	16	
304	23.245	11.705	4.558	394	102	33	
305	23.274	20.621	1.427	417	23	33	
306	23.660	7.336	0.962	886	31	8	
307	24.120	-3.575	4.011	426	43	17	
308	24.132	17.674	1.906	460	28	30	
309	24.671	11.224	2.197	461	29	29	
310	25.195	17.314	5.274	488	155	28	
311	25.298	13.253	2.751	216	21	34	
312	25.348	7.543	2.171	371	41	28	
313	25.533	9.375	1.130	759	29	12	
314	25.642	10.723	3.577	262	32	34	
315	25.967	2.582	1.155	957	110	9	UPK 28
316	26.055	6.496	2.837	642	71	16	
317	26.117	21.985	1.393	457	24	29	
318	26.670	-12.115	2.714	656	49	16	
319	26.981	7.673	1.101	728	45	12	
320	28.783	3.082	10.166	455	2388	18	Serpens
321	28.883	-2.200	1.035	822	30	12	
322	29.051	3.646	2.562	448	32	28	Serpens
323	29.161	-4.984	2.757	418	41	28	
324	29.301	8.369	3.636	381	67	28	
325	29.364	2.870	0.976	920	123	8	Serpens South
326	29.378	23.445	2.532	407	70	29	
327	29.851	27.132	2.553	501	35	36	
328	30.079	-8.742	10.714	320	141	34	
329	30.148	-0.858	2.209	449	27	30	
330	30.444	17.313	4.708	364	399	29	IC 4665
331	30.581	-20.980	4.472	455	103	36	Alessi 10
332	30.590	0.258	4.543	645	610	16	Serpens Low
333	30.725	3.336	0.738	887	28	8	
334	30.899	12.728	13.064	539	1571	25	Collinder 350
335	31.418	-12.065	5.227	410	62	29	
336	31.473	-5.095	2.310	412	22	36	
337	31.510	-2.244	1.028	1086	32	9	
338	31.565	-5.182	2.201	413	36	28	
339	32.135	-13.356	3.233	461	109	29	
340	32.182	-14.335	6.006	377	50	33	
341	32.213	-3.206	2.715	479	36	25	
342	32.278	-6.281	8.525	455	223	28	
343	33.233	-0.906	1.709	831	57	12	
344	33.890	0.643	2.543	610	130	13	[MML2017] 2399
345	34.128	7.945	3.032	386	46	19	NGC 6633
346	34.582	0.182	1.223	1092	73	7	
347	35.048	2.629	0.830	661	24	15	
348	35.243	-11.303	2.622	442	24	36	
349	35.727	7.681	1.630	566	21	27	
350	35.728	-0.701	2.667	838	92	12	
351	36.560	16.375	3.856	465	37	36	
352	36.603	7.447	6.182	433	318	29	IC 4756
353	37.527	-17.166	2.093	377	28	29	
354	38.236	5.959	3.396	708	85	26	
355	38.385	-17.095	4.095	443	38	36	
356	39.213	-3.615	4.999	553	171	25	
357	39.555	-2.143	0.869	841	27	12	
358	40.706	3.473	3.521	482	61	36	

Table 3. continued.

ID	l [deg]	b [deg]	r_{50} [deg]	d [pc]	N	Flag	Name
359	40.799	6.050	9.103	559	638	25	IC 4756
360	41.590	-2.991	7.016	434	53	28	
361	42.149	-7.147	5.254	573	108	27	
362	43.430	2.670	5.727	573	128	27	
363	43.474	2.776	4.315	563	114	18	
364	43.677	-8.542	4.309	784	192	26	UBC 14
365	44.216	1.567	2.250	790	63	16	
366	44.670	-0.548	3.496	456	89	36	
367	45.022	-8.433	2.742	465	45	36	
368	46.105	-9.918	7.453	494	178	36	
369	46.311	-1.171	1.509	426	36	18	
370	46.503	16.229	14.058	392	2270	29	Alessi 19
371	46.549	23.690	1.808	616	35	27	
372	48.061	5.016	2.203	555	22	28	
373	49.914	3.894	3.608	547	108	18	
374	50.044	-16.059	2.926	482	34	28	
375	51.950	-11.792	5.117	437	187	36	
376	53.239	1.424	1.936	1229	386	11	
377	54.433	4.227	3.396	449	30	36	
378	55.400	5.146	11.010	522	3182	28	Alessi 62
379	57.264	-25.172	1.222	873	30	12	
380	57.515	-2.523	0.856	807	21	16	
381	57.776	2.491	2.598	991	112	15	
382	58.660	-21.122	1.745	497	31	25	
383	60.821	-1.193	1.019	1212	118	11	
384	62.213	-9.437	1.735	786	28	16	
385	63.459	0.818	3.912	620	29	27	ASCC 105
386	64.339	13.488	13.797	376	2791	29	ASCC 101
387	65.115	-19.330	2.100	621	40	27	
388	65.296	-11.736	2.448	308	33	29	UPK 88
389	65.977	1.880	2.529	647	37	27	
390	66.056	3.696	3.213	333	42	22	
391	66.153	-3.123	1.194	1326	134	2	65.78-2.61
392	66.202	7.234	1.907	519	31	28	
393	67.547	-1.482	3.840	666	55	27	UPK 93
394	68.445	2.589	2.280	1002	89	12	
395	68.699	-6.433	5.639	455	74	33	
396	71.161	-2.629	1.931	790	33	16	
397	71.422	6.958	5.625	549	454	36	Teutsch 35
398	74.560	21.213	2.603	590	25	28	
399	75.851	-5.949	4.010	511	37	36	
400	76.257	0.471	15.871	530	2556	36	NGC 6991
401	76.935	-8.164	5.146	611	142	28	UPK 113
402	77.261	0.402	7.218	361	275	33	Roslund 6
403	78.223	0.310	2.633	1018	381	12	CygnusX
404	78.290	2.593	3.026	1068	936	12	CygnusX
405	78.753	1.778	2.293	1339	616	7	Ass Cyg OB 9
406	79.435	-9.117	3.218	735	105	27	UPK 113
407	79.668	-4.738	10.506	546	346	28	North America
408	79.691	7.204	4.478	727	105	27	
409	79.867	-0.908	0.886	1557	167	1	[LK2002] C110
410	79.882	0.401	2.104	1341	551	2	CygnusX
411	81.022	4.359	6.587	530	99	28	
412	81.941	-0.456	0.692	1013	50	12	
413	81.954	2.539	0.916	1356	71	10	
414	82.086	-2.278	0.829	1144	37	10	
415	83.036	6.149	11.869	372	1507	29	RSG 5
416	83.171	-2.313	0.917	1067	42	9	
417	83.831	0.905	0.900	1231	36	7	
418	84.737	-0.420	4.926	851	1588	13	North America

Table 3. continued.

ID	l [deg]	b [deg]	r_{50} [deg]	d [pc]	N	Flag	Name
419	86.386	2.697	4.512	650	61	27	
420	87.174	10.292	2.666	481	34	30	Alessi Teutsch 11
421	87.748	0.677	2.567	294	41	34	
422	87.823	-9.970	3.670	519	51	36	
423	87.938	20.018	2.250	335	36	34	UBC 1
424	87.965	1.658	4.617	565	87	28	L988
425	88.350	-1.717	5.322	767	1048	16	NGC 7039
426	88.872	-11.760	1.919	555	31	36	
427	90.660	0.894	1.725	477	22	29	
428	90.664	2.720	5.617	642	568	18	L977
429	90.769	-17.259	2.576	474	36	36	
430	91.008	2.356	2.953	980	327	9	Gulliver 48
431	91.910	-0.083	2.630	543	28	29	
432	92.124	3.488	3.307	606	76	25	Northern Coalsack
433	92.530	8.194	3.470	532	28	36	
434	92.653	2.529	0.950	1129	46	9	CygOB7 CO Complex
435	93.547	-0.058	2.039	574	27	28	
436	93.634	5.793	4.962	415	45	32	
437	93.684	17.260	3.181	614	43	27	
438	94.131	-1.235	11.806	480	1751	29	L988
439	94.371	-5.506	3.233	784	395	13	IC5146
440	95.123	7.421	8.881	340	651	32	
441	95.654	5.895	1.940	504	48	28	
442	96.430	-3.406	3.943	551	46	25	IC5146
443	96.564	14.640	2.088	563	31	25	
444	96.684	-3.192	4.911	297	70	33	
445	96.762	-15.032	11.268	548	2367	27	Lac OB1
446	98.435	7.783	1.355	886	253	16	UBC 385
447	98.452	12.017	7.820	492	350	28	
448	99.236	4.733	7.407	945	3140	12	IC 1396
449	99.350	6.383	1.676	954	47	12	IC1396
450	99.676	6.536	3.715	536	92	30	
451	100.073	1.535	4.001	509	114	36	
452	100.352	8.959	3.094	448	34	33	
453	100.562	8.694	1.147	1280	193	6	UBC 386
454	100.786	-1.069	6.282	336	185	33	
455	100.791	13.762	5.890	392	50	33	Cepheus
456	100.925	24.845	2.907	193	29	32	
457	101.146	-1.650	4.276	512	350	28	
458	101.182	-5.123	3.843	650	47	27	UPK 167
459	101.195	9.501	6.977	503	120	30	
460	101.457	0.282	6.965	252	82	34	
461	102.448	-13.775	6.439	580	967	27	Alessi 37
462	102.626	15.423	2.224	577	48	36	
463	102.657	1.096	3.750	391	43	33	
464	103.394	-4.251	6.246	243	168	34	ASCC 123
465	104.508	13.950	3.039	350	124	17	[YDM97] CO 14
466	104.998	9.267	3.333	308	26	31	
467	105.254	2.811	3.309	531	47	36	
468	105.443	8.084	6.038	481	388	29	
469	105.807	19.319	4.962	184	41	31	
470	106.032	-9.281	3.239	518	101	36	UPK 185
471	107.567	14.062	2.299	231	25	30	
472	108.116	16.321	4.769	411	85	33	Cepheus
473	108.630	14.427	8.384	529	194	36	L1228D
474	108.911	4.359	9.748	923	11445	15	Cepheus
475	109.119	2.553	3.853	438	30	32	
476	109.331	-1.212	12.055	469	2900	28	RSG 8
477	109.417	-1.468	7.792	324	152	33	
478	109.463	9.297	4.393	445	40	33	

Table 3. continued.

ID	l [deg]	b [deg]	r_{50} [deg]	d [pc]	N	Flag	Name
479	109.847	-3.187	3.020	473	49	30	
480	109.935	-14.284	5.122	456	520	28	Aveni Hunter 1
481	110.265	-0.303	2.768	238	26	34	
482	110.620	-2.902	1.761	415	21	33	
483	111.128	19.042	4.614	390	157	19	Cepheus
484	111.822	-1.613	3.671	433	39	29	
485	111.934	10.230	4.880	556	51	30	L1228D
486	112.344	13.607	8.568	358	577	19	L1228D
487	112.509	4.710	6.491	386	656	29	ASCC 127
488	112.800	15.862	3.350	563	85	28	
489	113.474	26.893	1.961	640	22	27	
490	113.542	15.296	3.376	483	75	28	L1228D
491	113.566	7.847	3.243	520	31	36	
492	115.986	9.653	4.939	537	152	36	L1228D
493	116.047	6.953	2.416	511	24	36	
494	116.119	29.231	1.293	501	26	30	
495	116.553	16.503	3.660	165	33	30	
496	116.712	8.793	2.606	333	22	24	
497	116.954	-7.113	2.337	416	135	28	
498	117.775	-3.639	6.049	431	476	28	Alessi 20
499	118.307	-15.249	2.227	439	28	36	
500	119.410	2.985	1.310	730	73	13	UPK 237
501	121.375	3.393	0.931	715	36	13	
502	121.382	-2.965	5.632	316	111	33	
503	121.880	-0.930	5.700	562	258	25	
504	122.334	16.652	2.531	158	27	31	
505	122.351	-12.204	3.285	464	89	36	
506	123.047	2.936	4.647	559	57	36	
507	123.800	6.063	5.121	500	56	36	
508	124.710	9.267	7.573	495	224	36	
509	125.617	-15.150	3.445	414	45	36	
510	126.202	-1.462	3.386	476	43	30	
511	126.541	-4.783	2.988	467	30	33	
512	126.737	-3.404	1.698	487	24	25	
513	126.833	-0.808	2.335	1003	287	6	L1306
514	127.769	1.932	1.897	485	23	30	
515	129.419	13.879	3.715	427	43	30	
516	130.046	-1.585	10.935	402	361	33	Stock 2
517	130.726	11.084	4.914	936	804	12	L1340
518	131.163	11.883	3.436	314	29	32	
519	132.286	-1.463	5.074	450	75	33	Stock 2
520	133.580	13.348	5.353	394	59	33	Polaris
521	133.668	3.798	2.095	508	21	36	
522	134.828	16.222	2.631	538	46	36	
523	136.008	-0.420	2.271	424	26	33	
524	136.204	-7.898	3.510	414	51	29	
525	136.724	-16.091	3.295	404	56	36	
526	137.256	-5.620	1.642	433	21	36	
527	137.474	8.339	2.394	452	48	29	
528	140.604	-6.082	4.529	336	30	31	UPK 296
529	141.113	1.692	1.458	1126	237	7	
530	142.173	1.953	4.116	1134	510	11	
531	143.626	-0.025	4.994	407	110	30	
532	143.661	7.684	1.723	1084	380	12	NGC 1502
533	143.665	-15.816	6.010	462	186	30	NGC 1039
534	144.812	1.258	7.726	312	77	34	
535	145.037	7.159	4.457	511	76	28	
536	145.567	-8.300	3.291	512	52	36	
537	145.649	-2.571	6.813	329	129	34	
538	145.915	13.155	3.551	484	40	36	

Table 3. continued.

ID	l [deg]	b [deg]	r_{50} [deg]	d [pc]	N	Flag	Name
539	147.247	-17.515	5.761	206	59	35	UPK 303
540	147.504	-6.461	8.867	174	414	34	Melotte 20
541	147.577	-1.832	2.621	286	21	34	
542	148.957	-0.721	2.084	1165	493	10	NGC 1444
543	149.073	15.520	3.507	492	44	36	
544	149.142	-24.809	1.424	400	24	30	
545	149.179	1.093	3.270	454	39	36	
546	151.243	9.446	2.361	392	22	33	
547	152.662	-9.714	0.916	1039	48	6	
548	153.102	-5.726	6.401	464	132	36	
549	154.222	12.280	7.849	506	274	28	UBC 8
550	154.998	-13.863	2.019	456	33	36	
551	156.640	9.786	6.365	451	114	36	UBC 8
552	157.382	-23.283	2.951	395	40	36	
553	157.984	-3.850	7.377	331	144	32	
554	160.790	-15.812	11.430	334	2661	19	IC 348
555	160.852	-1.558	2.039	418	22	28	
556	163.911	0.673	3.643	1238	365	11	ASCC 12
557	165.339	-8.928	5.498	544	429	18	NGC 1579
558	165.791	22.088	4.047	560	94	25	UPK 350
559	165.860	8.454	5.142	489	82	36	
560	166.196	-4.622	2.810	480	38	28	
561	166.366	-13.774	2.158	449	31	36	
562	166.573	-23.406	5.882	137	296	35	Melotte 22
563	167.663	-10.478	6.740	450	101	28	NGC 1579
564	167.756	-3.460	4.083	347	184	33	RSG 1
565	168.332	-12.907	5.084	352	85	32	
566	170.726	4.638	10.057	456	314	36	COIN-Gaia 13
567	170.731	-22.066	2.678	365	27	36	
568	171.144	-7.761	2.765	468	38	36	
569	171.881	4.649	3.693	435	44	36	
570	172.114	-15.302	4.551	132	112	21	Taurus
571	172.352	-28.669	2.649	227	22	32	
572	172.861	-22.497	2.946	123	30	24	
573	173.338	-8.026	2.852	159	34	14	
574	175.151	-0.770	2.912	439	37	36	
575	175.523	-16.567	2.293	164	22	20	Taurus
576	176.097	-16.340	3.085	123	21	32	
577	179.344	-19.869	2.313	146	27	14	
578	180.345	-8.937	2.533	372	25	32	
579	180.820	-6.009	3.875	171	88	25	
580	180.913	-6.770	5.164	278	57	31	
581	181.431	-3.841	3.896	770	363	12	Gulliver 22
582	181.696	15.476	2.261	497	32	36	
583	182.020	-12.956	2.009	423	29	33	
584	182.096	-10.804	13.453	428	1856	28	
585	182.276	-26.673	4.931	295	78	22	
586	182.618	-3.297	7.238	504	127	27	
587	183.117	4.770	4.120	492	33	36	
588	183.174	-15.571	4.009	123	25	32	
589	183.368	-2.763	3.263	238	29	34	
590	184.113	-0.602	2.894	430	31	29	
591	187.731	-21.132	2.025	429	80	36	NGC 1662
592	188.276	-2.474	2.838	201	35	30	
593	188.824	-12.715	2.647	211	26	34	
594	189.509	-27.298	6.073	169	37	34	
595	190.308	-3.692	8.230	652	274	26	COIN-Gaia 25
596	191.258	-17.962	5.196	368	294	29	UPK 385
597	191.930	-6.874	5.337	294	74	32	
598	193.354	-8.525	3.972	292	65	32	

Table 3. continued.

ID	l [deg]	b [deg]	r_{50} [deg]	d [pc]	N	Flag	Name
599	194.322	-2.785	4.822	422	36	36	
600	195.102	-12.093	7.639	408	1576	25	Orion Lam
601	195.187	-2.361	3.883	212	127	34	
602	198.915	-11.637	3.884	454	199	25	Orion
603	199.719	-8.593	8.645	399	492	28	Orion Lam
604	203.046	1.827	10.006	726	1916	15	NGC2264
605	205.945	-23.383	2.198	333	26	25	
606	206.377	-19.086	17.199	382	14832	25	Orion
607	206.438	-1.903	2.025	1571	810	3	Rosette
608	207.126	-7.044	7.262	335	441	29	
609	209.893	-10.950	7.282	472	275	36	NGC 2184
610	209.921	-1.553	4.507	385	31	36	
611	213.130	8.080	2.438	465	44	36	
612	213.340	-22.854	3.270	284	33	24	
613	214.562	-12.553	5.982	884	1272	12	Mon R2
614	215.533	-7.983	13.427	372	1703	30	NGC 2232
615	216.987	-24.800	4.640	281	48	29	
616	217.508	-8.133	2.739	212	27	31	
617	218.741	-2.154	4.131	292	445	30	
618	219.104	-8.675	3.935	999	620	6	Mon R2
619	221.012	-10.347	3.022	445	21	36	
620	221.023	-5.593	5.913	304	155	29	
621	221.141	1.682	2.393	485	28	30	
622	221.306	-16.790	3.742	689	485	16	UPK 445
623	223.698	-4.002	4.486	805	57	26	
624	223.946	-0.249	8.022	577	343	27	Alessi 21
625	224.298	-22.407	3.063	201	39	32	
626	224.621	-2.244	3.027	1233	1709	10	BRC 27
627	225.298	-21.186	2.405	373	27	33	
628	226.521	-12.094	16.429	392	3280	29	
629	228.053	-4.329	5.307	343	55	32	
630	230.973	-10.450	1.013	814	28	16	NGC 2287
631	230.995	3.061	6.238	500	347	36	NGC 2422
632	232.760	-4.298	5.072	283	67	34	
633	237.327	-9.186	9.878	818	4416	26	ASCC 32
634	237.898	-11.168	5.777	398	388	29	
635	238.406	-5.159	2.269	1353	879	10	NGC2362
636	239.623	-1.752	1.480	1424	96	11	
637	239.933	-17.109	3.286	272	40	34	
638	240.256	-3.215	4.038	280	50	32	
639	241.963	-9.944	1.472	293	22	32	
640	244.621	-2.737	9.095	569	1849	27	Haffner 13
641	246.140	-4.798	3.067	225	33	34	
642	246.221	-10.606	11.418	380	1389	29	Collinder 135
643	247.158	-6.200	2.631	655	24	27	
644	247.270	3.179	3.463	393	57	29	
645	248.186	-14.704	1.134	550	30	36	
646	248.700	-0.080	1.206	1205	72	6	
647	248.924	-13.355	5.236	279	355	32	UBC 7
648	251.662	-0.341	7.688	519	1958	27	BH 23
649	252.611	-7.382	6.355	194	174	34	NGC 2451A
650	253.198	-7.499	9.513	401	2826	29	NGC 2451B
651	256.096	-18.812	4.205	190	52	32	
652	256.335	-2.045	4.507	637	520	27	Gulliver 10
653	256.814	-4.034	4.510	870	391	16	
654	257.112	20.949	1.560	486	23	36	
655	257.548	-8.913	4.358	269	47	34	
656	258.160	-8.400	3.095	408	140	30	
657	259.288	3.593	5.400	674	267	27	Teutsch 38
658	259.571	13.678	3.032	468	29	36	

Table 3. continued.

ID	l [deg]	b [deg]	r_{50} [deg]	d [pc]	N	Flag	Name
659	260.211	-6.824	5.378	494	43	36	
660	260.224	-8.691	6.145	332	625	30	VelaOB2
661	261.603	1.057	5.671	973	2797	12	Vela C
662	261.858	-8.321	13.343	398	6001	25	Pozzo 1
663	262.069	-2.980	3.481	531	28	36	
664	262.449	-10.136	2.958	167	25	32	
665	263.394	-3.152	6.854	732	354	27	IC 2395
666	263.889	-19.699	6.355	573	199	36	UPK 524
667	264.272	-26.379	1.659	510	28	36	
668	264.587	1.894	2.165	1083	111	11	Vela C
669	265.335	-19.187	8.048	214	127	32	
670	267.047	-21.762	2.873	526	44	36	
671	267.183	5.875	4.114	661	115	27	
672	267.246	3.984	2.851	187	40	34	Platais 9
673	267.361	-5.466	6.612	371	407	30	UPK 535
674	267.492	-0.175	2.418	885	155	12	
675	267.850	-0.066	2.034	1225	158	11	
676	268.813	1.996	2.294	777	112	15	